Dust agglomeration

Jürgen Blum

Dust agglomeration

JÜRGEN BLUM*

Institut für Geophysik und extraterrestrische Physik, Technische
Universität zu Braunschweig, Mendelssohnstr. 3, 38106 Braunschweig,
Germany

Dust agglomeration plays an important role in astrophysics and atmospheric
sciences as well as in industrial processes. This article reviews the current
knowledge of the physical interactions that lead to particle sticking in gaseous
environments as well as the morphologies of the resulting dust aggregates. With
this basic knowledge of dust–dust interactions, the development of ensembles
of interacting dust particles can be treated using Smoluchowski's equation.
Considering analytical solutions and simplified physical conditions, the
temporal evolution and the mass distribution functions of dust aggregates are
discussed. Based on this, general dust aggregation phenomena can be modelled
and introduced into more complex scenarios.

Contents

*Email: j.blum@tu-bs.de

1. Introduction and motivation

This review article is intended to summarise the knowledge on 'dust agglomeration' (or 'dust aggregation' which will be used synonymously throughout this article), i.e. a process in which small solid particles collide and stick in a gaseous (or vacuum) environment (figure 1). As will be shown later, one must distinguish between two different possible outcomes. Either the two colliding dust aggregates stick at their point of first contact (figure 1 top) and form a new dust agglomerate which preserves the shapes of the educts or, due to restructuring processes during the collision, an aggregate is formed that does not resemble the morphologies of the two collision partners (figure 1 middle). It should also be mentioned that very energetic collisions can also lead to the (partial or full) destruction of the colliding aggregates for which the term 'fragmentation' is used (figure 1 bottom). As the author's background is in astrophysics, dust aggregation will be treated for systems in which the local (but not necessarily the global) mass density is dominated by the dust particles (and not by the carrier medium). Thus, the processes presented and discussed here are applicable in astrophysics; some aspects also apply to aerosol science, atmospheric physics and nanoparticle physics. An overview on aerosols is given by Friedlander [1]. Colloidal aggregation (i.e. aggregation in a liquid medium) will not be considered due to the importance of the carrier medium and the formation of double layers. Due to these restrictions and the author's personal background, this review is biased and far from being exhaustive. The prime intention of this article is to give an overview of the problem of dust aggregation and possible solutions to dust-aggregation problems, to describe the physics behind the phenomenon of dust aggregation, and to gain a thorough understanding of aggregation kinetics. However, in addition to that, this work shall also be utilitarian and 'applicable', i.e. the readers (scientists and students) will find formulae and recipes for their own applications in dust aggregation.

One of the primary questions in the field of dust aggregation is: why and when do dust particles stick? In the following, it will be assumed that the dust particles are
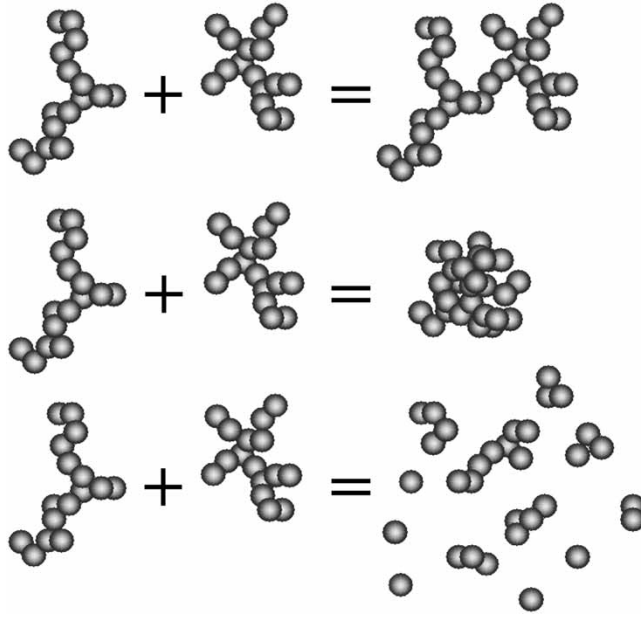
Figure 1. Principles of the interaction between dust agglomerates. The top panel shows the simple hit-and-stick behaviour of dust agglomeration; the central panel shows a sticking event between two dust agglomerates which does not preserve the agglomerate structures, i.e. which leads to agglomerate compaction; the bottom panel demonstrates how fragmentation in a collision between dust agglomerates might look.

part of an ensemble of small solid grains† with a given size (or mass) distribution and number density. Collisions between the dust particles should be possible and can be due to Brownian motion, relative drift motions, turbulence, mutual long-range attraction (electric or magnetic forces) or other external forces. It will be investigated under what circumstances these collisions lead to the sticking of the dust particles/ aggregates and what the physical processes behind particle sticking are. When considering many sticking collision events within an ensemble of dust particles, questions on aggregate morphologies, mass distribution functions and the temporal evolution of the mean aggregate mass will also be addressed. Typical grain sizes for astrophysical applications are $\lesssim 1\,\mu m$. However, nanoparticles (although clearly present in space) will not explicitly be treated due to the relative higher importance (in terms of total mass) of dust grains at the upper end of the size range. A basic difference between aggregation processes in nano- and micro-particle systems is that the contact area between microparticles is much smaller than the particles' cross sections (see section 5.2), whereas this is not the case for nano-particles. In addition to that, for micro-particles the threshold velocity for particle sticking is much smaller

---

†Examples for small solid grains (frequently termed monomers) are soot, aerosols and interstellar dust.

than the sound speed in the particle material. Nano-particles, on the other side, even stick to one another at velocities above 1 km/s [2] which is close to the sound speed in solid materials. Thus, inter-particle sticking and particle shattering in mutual collisions are likely to coincide for nano-particles whereas these processes are widely separated for micro-particles.

This review is structured such that in the following section 2, the mean-field approach to dust agglomeration will be presented. It will be started with Smoluchowski's growth equation and its solutions, developing from simple, monodisperse systems, which already reveal many interesting features, to complex systems with broad size distributions. In section 3, an introduction to fractal and nonfractal dust agglomerates will be given and the implications of the aggregate structures on the form of the growth equation will be derived. Section 4 gives some experimental examples that validate the applicability of the mean-field approach to the problem of dust agglomeration. Section 5 is an introduction to the physics of collision interactions between dust particles and dust agglomerates. Methods for the observation and analysis of dust agglomeration are shown in section 6. Finally, section 7 presents an astrophysical application of dust agglomeration.

2. The mean-field theory of dust agglomeration

In this section, it is assumed that the system under investigation consists of an ensemble of dust particles in which agglomeration takes place. This particle ensemble is so large that statistical averages (e.g. of the agglomerate mass) can be defined. Also the volume of interest in which the agglomeration takes place is assumed to be sufficiently large so that the number of dust agglomerates of all masses can also be treated in a statistical sense. It will be shown that a simple rate equation describes those cases in which two particles stick upon a collision with a specified probability and in which the collision rate is independent of the grains' orientation (section 2.1). This rate equation, introduced by von Smoluchowski [3] is a first-order nonlinear differential equation whose solutions will be addressed in the subsequent subsection 2.2. At first, it is assumed that the growing dust particles obtain a monodisperse mass distribution (section 2.2.1) which will lead to a simple-to-solve differential equation. Section 2.2.2 will show that this assumption is not fulfilled in any physical system. However, the conclusions drawn from the simplified assumption of monodispersity for the temporal development of the mean particle mass still holds for more generalised systems. In section 2.2.2, some analytical solutions of the discrete Smoluchowski equation will be treated, before general aspects of its solutions, such as the scaling behaviour and the self-similarity of the solutions will be considered. As many physical systems have sources and/or sinks of particles, some general polydisperse solutions without the constraint of mass conservation are presented in section 2.2.3. In section 2.3, anisotropic systems, such as those caused by grain alignment by gas drag (section 2.3.1), magnetic force (section 2.3.2) and electric force (section 2.3.3) will be treated, which might considerably enhance the growth rate of dust aggregates.

2.1. *Isotropic systems and Smoluchowski's growth equation*

This review will begin with systems of dust particles in which all interactions and motions of the dust particles are spatially isotropic. In most applications the time between two successive collisions is longer than the contact time, so it is assumed that the agglomeration proceeds stepwise by pair collisions. Let $n(m, t)\mathrm{d}m$ be the number density of dust particles† with masses between m and $m + \mathrm{d}m$ at time t. Then the number of collisions per unit volume and unit time between two dust aggregates in the mass ranges $m_1 \ldots m_1 + \mathrm{d}m_1$ and $m_2 \ldots m_2 + \mathrm{d}m_2$ is given by

$$v(m_1, m_2) = f(m_1, m_2)\, n(m_1)\, n(m_2)\mathrm{d}m_1\mathrm{d}m_2, \tag{1}$$

where

$$f(m_1, m_2) = \sigma(m_1, m_2)\, v(m_1, m_2) \tag{2}$$

denotes the collision frequency and $\sigma(m_1, m_2)$ and $v(m_1, m_2)$ are the collision cross section and the collision velocity, respectively. Equation 2 assumes ballistic collisions, i.e. collisions for which the aggregates are on linear trajectories in the vicinity of the collision point.

If the sticking probability for the collision

$$\text{particle}(m_1) + \text{particle}(m_2) \longrightarrow \text{particle}(m_1 + m_2), \tag{3}$$

is given by $\beta_\mathrm{a}(m_1, m_2; v)$, the temporal evolution of number densities can be described by the integral form of Smoluchowski's equation [3]‡

$$\frac{\partial n(m, t)}{\partial t} = \frac{1}{2}\int_0^m K_\mathrm{a}(\bar{m}, m - \bar{m})n(\bar{m}, t)n(m - \bar{m}, t)\mathrm{d}\bar{m}$$
$$- n(m, t)\int_0^\infty K_\mathrm{a}(\bar{m}, m)n(\bar{m}, t)\mathrm{d}\bar{m}. \tag{4}$$

Here, $K_\mathrm{a}(m_1, m_2) = \beta_\mathrm{a}(m_1, m_2; v)\, f(m_1, m_2)$ is the reaction kernel for agglomeration of the coagulation equation 4. The first term on the RHS of equation 4 describes the rate of sticking collisions between dust particles of masses $\bar{m}$ and $m - \bar{m}$ whose combined masses are m (gain in number density for the mass m), whereas the second term on the RHS of equation 4 denotes a loss in the number density for the mass m due to sticking collisions between particles of mass m and mass $\bar{m}$. The factor $1/2$ in the first term on the RHS of equation 4 accounts for the fact that each pair collision is counted twice in the integral. Smoluchowski's equation conserves the total mass in the system, i.e.

$$\int_0^\infty n(m, t)m\, \mathrm{d}m = \text{const.} \tag{5}$$

---

†In the following, the expression 'dust particle', 'dust aggregate' and 'dust agglomerate' will be used synonymously and it will not be distinguished between single solid grains and aggregates thereof.

‡For the validity of equation 4, it is required that the number densities are not too high so that only binary collisions are important. Equation 4 is also termed *growth equation*, *coagulation equation* or *rate equation*.

Large-scale numerical treatments of agglomeration processes have shown that Smoluchowski's equation can be used for the description of agglomeration problems for low [4, 5] as well as for high [6] number concentrations of particles. However, as Smoluchowski's rate equation does not contain any spatial information, it is only valid for homogeneously mixed systems. Thus, when spatial inhomogeneities or fluctuations in the size distribution of dust aggregates occur, Smoluchowski's equation cannot be applied. In general, the mixing timescale in the particulate system must be shorter than the growth timescale for a reasonable application of the mean-field approach by a rate equation [7].

However, not all collisions necessarily lead to agglomeration. If one assumes that a fraction $\beta_f(m_1, m_2; v)$ of collisions between aggregates of masses m_1 and m_2 lead to fragmentation, i.e. to a distribution of smaller masses, one can set up a rate equation for fragmentation

$$
\left(\frac{\partial n(m, t)}{\partial t}\right)_f = \frac{1}{2}\int_0^\infty \int_0^\infty P(m; \bar{m}, m'; v)K_f(\bar{m}, m')n(\bar{m}, t)n(m', t)\mathrm{d}\bar{m}\mathrm{d}m'
$$
$$
- n(m, t)\int_0^\infty K_f(\bar{m}, m)n(\bar{m}, t)\mathrm{d}\bar{m}. \tag{6}
$$

The first term on the RHS of equation 6 describes the formation of fragments of mass m through all possible destructive collisions between two larger aggregates. Here, $P(m; \bar{m}, m'; v)\mathrm{d}m$ describes the efficiency with which a collision between two aggregates with masses $\bar{m}$ and m' will produce fragments in the mass range $m \ldots m + \mathrm{d}m$. The fragmentation kernel is given by $K_f(m_1, m_2) = \beta_f(m_1, m_2; v) f(m_1, m_2)$. The second term on the RHS of equation 6 describes a catastrophic collision in which one of the aggregates has the mass m.

In general, the ensemble of dust particles and aggregates is not an isolated system but has sources and sinks of particles which can be expressed by the time-dependent gain and loss rates from all processes other than collisions for aggregates with masses in the range $m \ldots m + \mathrm{d}m$, $G(m, t)\mathrm{d}m$ and $L(m, t)\mathrm{d}m$. Causes for gains or losses of particles can be condensation/evaporation or transport processes. Taking everything together, the rate equation encompassing agglomeration, fragmentation and particle gains or losses becomes

$$
\frac{\partial n(m, t)}{\partial t} = \frac{1}{2}\int_0^m K_a(\bar{m}, m - \bar{m})n(\bar{m}, t)n(m - \bar{m}, t)\mathrm{d}\bar{m}
$$
$$
- n(m, t)\int_0^\infty K_a(\bar{m}, m)n(\bar{m}, t)\mathrm{d}\bar{m}
$$
$$
+ \frac{1}{2}\int_0^\infty \int_0^\infty P(m; \bar{m}, m; v')K_f(\bar{m}, m')n(\bar{m}, t)n(m', t)\mathrm{d}\bar{m}\mathrm{d}m' \tag{7}
$$
$$
- n(m, t)\int_0^\infty K_f(\bar{m}, m)n(\bar{m}, t)\mathrm{d}\bar{m}
$$
$$
+ G(m, t) - L(m, t).
$$

2.2. *Solutions to Smoluchowski's equation for isotropic systems*

2.2.1. Monodisperse systems. Equation 7 is complex and has in general no analytic solution. However, with a few assumptions and simplifications valuable conclusions can be drawn from the rate equation.

(i) First of all, going back to equation 4, neither fragmentation nor gains or losses of particles will be considered.

(ii) Secondly, it is assumed that all dust aggregates consist of smallest entities (monomer grains) with identical mass m_0. This means that an aggregate with mass m can also be expressed by the number of monomer grains,

$$i = \frac{m}{m_0}. \tag{8}$$

Using this, one can replace the integral form of Smoluchowski's equation (equation 4) by the discrete form,

$$\frac{\partial n(i, t)}{\partial t} = \frac{1}{2} \sum_{j=1}^{i-1} K_a(j, i-j) \, n(j, t)n(i-j, t) - n(i, t) \sum_{j=1}^{\infty} K_a(j, i)n(j, t), \tag{9}$$

where $n(i, t)$ denotes the number density of aggregates with 'mass' i. The reaction kernel of this rate equation for ballistic collisions is given by

$$K_a(j, i) = \beta_a(j, i; v) \, v(j, i) \, \sigma(j, i), \tag{10}$$

in which $\beta_a(j, i; v)$, $v(j, i)$ and $\sigma(j, i)$ are the sticking probability, the collision velocity and the cross section for collisions between agglomerates of monomer numbers i and j.

(iii) The next assumption is that the sticking probability for all collisions is approximated by

$$\beta_a(j, i; v) = 1. \tag{11}$$

This is justified for low-velocity collisions as will be shown in section 5.

(iv) Experimental and theoretical studies of growth kinetics have shown that many problems of dust aggregation can be described by a quasi-monodisperse growth (see sections 3 and 5), i.e. at a given time, the mass distribution function is rather narrow. Here, one can approximate this by the extreme assumption of a strictly monodisperse mass distribution, i.e. at a given time t only agglomerates with mass i are present; for all other masses $j \neq i$, $n(j) = 0$. The growth equation thus simplifies to

$$\frac{\partial n(i, t)}{\partial t} = -K_a(i, i)n^2(i, t). \tag{12}$$

(v) Strongly related to the previous assumption of monodispersity is the fact that dust agglomerates can be described by a mass-size relation of the form

$$i \propto s^{D_f}, \tag{13}$$

where s is the radius of the dust aggregate† and D_f denotes the fractal dimension (see section 3) with possible values in the range $D_f = 1, \ldots, 3$. Dust aggregates with $D_f = 1$ are chain-like, whereas agglomerates with $D_f = 3$ have a spheroidal, but possibly highly porous, structure. Computer simulations and laboratory experiments have shown that for the monodisperse case $D_f \lesssim 2$ (see section 3.1). In that case, the collision cross section for two dust aggregates can be approximated by [8]

$$\sigma(i, i) = \sigma_0 i^\beta, \tag{14}$$

with $\beta \approx 1$. Here, σ_0 is a scaling factor which is of the order of the collision cross section of the dust monomers. Equation 14 with $\beta \approx 1$ means that each individual monomer grain inside a dust aggregate contributes to the collision cross section, i.e. there are no 'hidden' particles inside an aggregate.

(vi) The collision velocities for fractal aggregates shall be approximated by a power law of the form

$$v(i, i) = v_0 i^\alpha, \tag{15}$$

where v_0 is given by the relative velocity between two monomer grains and the exponent α depends on the physics responsible for the aggregate–aggregate collisions. For $\alpha = 0$, all aggregates have identical collision velocities, in the case of $\alpha < 0$, the smaller aggregates have higher collision velocities than the larger ones, and for $\alpha > 0$, the larger agglomerates collide faster than the smaller grains.

With the assumptions (i) through (vi) and the respective approximations given in equations 11, 14 and 15, the growth equation 12 can be written

$$\frac{\partial n(i, t)}{\partial t} = -\sigma_0 v_0 i^\kappa(t) n^2(i, t), \tag{16}$$

where the relation $\kappa = \beta + \alpha$ was used. With this, the results can also be applied later for non-fractal particles. Here, κ is the exponent for the full kernel of the coagulation equation, i.e. $K_a(i, i) \propto i^\kappa$, and $i(t)$ is the time-dependent mass of the agglomerates in the system.

Assuming that the total spatial mass density of the agglomerates is constant over time, i.e.

$$n(i, t) \cdot i(t) = \mu_0 = \text{const.}, \tag{17}$$

or

$$i(t) \cdot \frac{\partial n(i, t)}{\partial t} + n(i, t) \cdot \frac{\partial i(t)}{\partial t} = 0, \tag{18}$$

one gets a differential equation for the mean agglomerate mass $i(t)$

$$\frac{\partial i(t)}{\partial t} = \mu_0 \sigma_0 v_0 \cdot i^\kappa(t). \tag{19}$$

---

†In many practical cases, the radius of gyration (see equation 72) is used as the radius of the aggregate.

With the characteristic collision time

$$\tau_c = \frac{1}{\mu_0 \sigma_0 v_0}, \tag{20}$$

one can derive from equation 19

$$\frac{\partial i(t)}{\partial t} = \frac{1}{\tau_c} \cdot i^\kappa(t). \tag{21}$$

Equation 21 has the general solution

$$i(t) = \left[(1 - \kappa) \left(\frac{t}{\tau_c} + c \right) \right]^{1/1-\kappa} \tag{22}$$

for $\kappa \neq 1$ and

$$i(t) = \exp\left(\frac{t}{\tau_c} + c \right) \tag{23}$$

for $\kappa = 1$, respectively. The constant c is determined by the initial conditions of the growth process considered. Figure 2 shows a few examples of equations 22 and 23 with $i(0) = 1$ and $\kappa = -\infty, 0, 1/2, 1, 2$.

For clarification of the results shown in equations 22 and 23, two examples of dust agglomeration, which will also be treated in section 5, will be considered.

Growth by ballistic Brownian motion ($\kappa = 1/2$). The Brownian motion of solid particles in gases is due to the statistical interaction of gas molecules with the dust particle. For thin gases, mutual collisions between dust aggregates caused by Brownian motion can be treated as ballistic (thus, equations 2 and 10 can be used
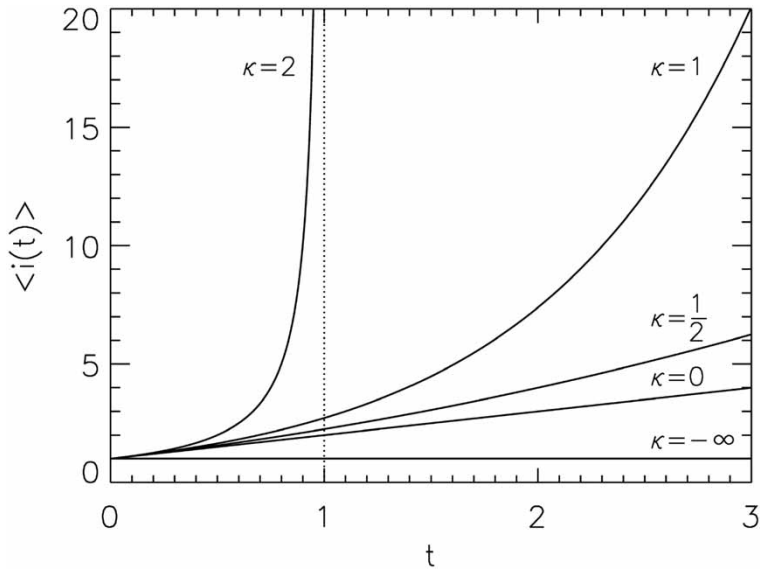

Figure 2. Solutions to equation (21) with $i(0) = 1$ and $\kappa = -\infty, 0, 1/2, 1, 2$.

although the overall motion of the dust grains is diffusive). Due to the equipartition of energy between the gas and the dust, one can write for the collision velocities between dust aggregates of mass i

$$v(i, i) \propto i^{-1/2} \tag{24}$$

Thus, one gets $\alpha = -1/2$ and $\kappa = 1/2$. With an assumed initial condition $i(0) = 1$, one gets from equation 22

$$i(t) = \left(\frac{t}{2\tau_c} + 1\right)^2. \tag{25}$$

The resulting growth curve is a parabola with a characteristic growth time scale of $\tau_g = 2\tau_c$. As will be shown later in section 5, this general finding is supported by experimental results.

Growth with constant collision velocity ($\kappa=1$). There are systems in which the relative velocities between the fractal dust agglomerates are independent of the agglomerate mass, e.g. in turbulent flows of rarefied gas and if the fractal dimensions $D_f \lesssim 2$ (see equation 13 for the definition of the fractal dimension) [9]. In that case, $\alpha = 0$ and $\kappa = 1$ so that the solution to the growth equation is given by equation 23. With an assumed initial condition $i(0) = 1$, one gets from equation 23

$$i(t) = \exp\left(\frac{t}{\tau_c}\right). \tag{26}$$

The growth time scale in that case is equal to the collision time scale of the monomers, i.e. $\tau_g = \tau_c$.

It should also be noted from equation 22 that there might be cases in which the mass of an aggregate diverges for a finite time. This is the case for $\kappa > 1$. As at least the assumption of monodispersity then breaks down, the implications will not be considered here but in the next paragraph.

2.2.2. Polydisperse systems with mass conservation. In the following, it will be investigated which analytic solutions to the rate equation (equation 9) are known and what one can learn from them about the resulting agglomerate mass spectra. There have been numerous publications about solving Smoluchowski's equation. Well-known examples are the articles by Ziff [10], Ernst [11], van Dongen and Ernst [12], Leyvraz [13], Jullien and Botet [14] and Smirnov [15]. Let us get back to equation 9 and normalise it such that the total number density of the monomer grains in the system is unity. One then gets with $c(i, t)$ for the normalised concentration

$$\frac{\partial c(i, t)}{\partial t} = \frac{1}{2}\sum_{j=1}^{i-1} K_a(j, i-j)\, c(j, t)c(i-j, t) - c(i, t)\sum_{j=1}^{\infty} K_a(j, i)c(j, t), \tag{27}$$

with

$$\sum_{i=1}^{\infty} i \cdot c(i, t) = 1. \tag{28}$$

There are a few cases known for which the normalised concentration function $c(i, t)$ can be derived analytically for arbitrary initial conditions. The results of those cases for an initially monodisperse mass distribution function $c(i, 0) = \delta_{i1}$ will be given below. These analytic solutions to Smoluchowski's equation primarily serve the academic purpose of displaying the shape and temporal behaviour of the mass distribution functions (figure 3) and to serve as benchmark tests for numerical solvers. However, it will be shown that some of the kernels result in bell-shaped (quasi-monodisperse) mass distribution functions (figures 3b and e) which can be compared to the respective monodisperse cases. Such a comparison to a simple model can give a deeper insight into the complex evolution of particulate systems.

Constant kernel $K_a(j, i) = 1$. The exact solution to equation 27 with monodisperse initial condition and a kernel

$$K_a(j, i) = 1 \tag{29}$$

is [16, 17]

$$c(i, t) = \frac{(t/2)^{i-1}}{(1 + t/2)^{i+1}} \tag{30}$$

(see figure 3a). If one defines the mean agglomerate mass through the moments M_1 and M_2 of the concentration function

$$M_1(t) = \sum_{i=1}^{\infty} i \, c(i, t) \tag{31}$$

and

$$M_2(t) = \sum_{i=1}^{\infty} i^2 \, c(i, t) \tag{32}$$

by†

$$\langle i(t) \rangle = \frac{M_2(t)}{M_1(t)}, \tag{33}$$

one gets with $c(i, t)$ from equation 30 the general solution for the mean agglomerate mass

$$\langle i(t) \rangle = M_2(0) + M_1^2 t \tag{34}$$

which is equivalent to

$$\langle i(t) \rangle = 1 + t \tag{35}$$

for $M_1 = 1$ and $M_2(0) = 1$. This means that the mean mass increases linearly with time. Although strict monodispersity is not observed (figure 3), the result for the mean agglomerate mass is in agreement with the earlier approximation, equation 22 with $\kappa = 0$, $c = 1$ and $\tau_c = 1$ (figure 2).

---

†M_1 in equation 33 is unity due to the normalisation in equation 28.
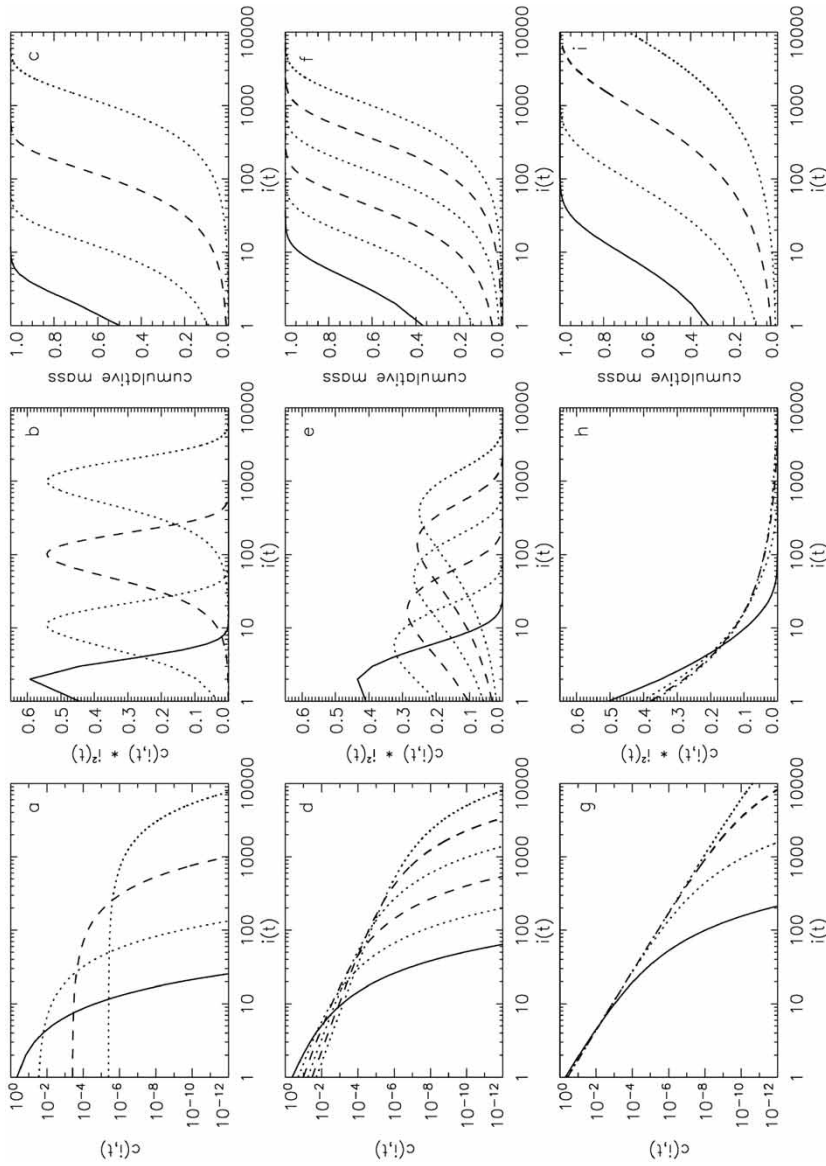
Figure 3. The concentration functions $c(i, t)$ (a, d, g) and the mass spectra $i^2 c(i, t)$ in differential (b, e, h) and cumulative (c, f, i) form for the kernels $K_a(j, i) = 1$ (a, b, c), $K_a(j, i) = j + i$ (d, e, f) and $K_a(j, i) = j \cdot i$ (g, h, i), respectively. The times of the curves are $t = 1, 10, 100, 1000$ for $K_a(j, i) = 1$, $t = 0.5, 1.0, 1.5, 2.0, 2.5, 3.0$ for $K_a(j, i) = j + i$, and $t = 0.68, 0.90, 0.97, 0.99$ for $K_a(j, i) = j \cdot i$. Mind the logarithmic scales in $i(t)$ and $c(i, t)$, whereas the differential and cumulative functions $c(i, t) \cdot i^2(t)$ are plotted linearly.
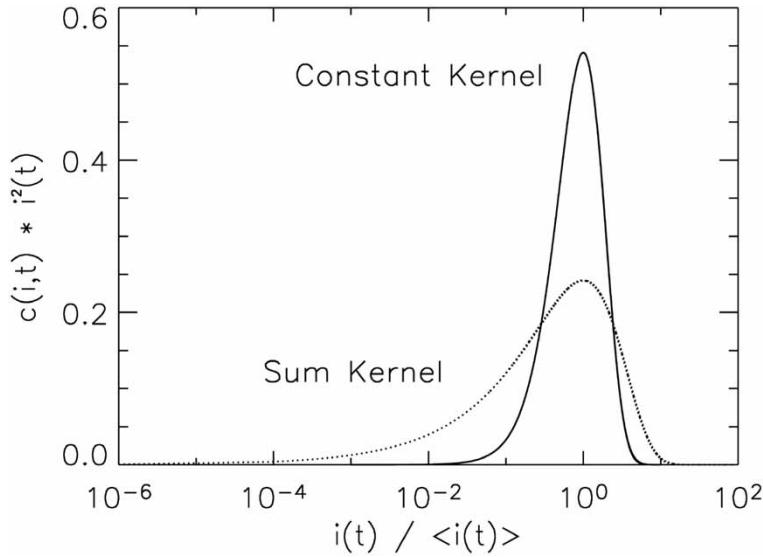
Figure 4. The self-similar solutions of the mass distribution function $c(i, t) \cdot i^2(t)$ for the kernels $K_a(j, i) = 1$ (solid line) and $K_a(j, i) = j + i$ (dotted line), respectively.

There are some interesting features in the mass distribution function, equation 30, which will be discussed briefly. First of all, $c(i, t) > c(j, t)$ for $i < j$ and all times t. This means that smaller agglomerates always dominate in particle number over larger agglomerates, although the mean mass increases. Secondly, for a given i, $c(i, t)$ goes through a maximum and decreases as $c(i, t) \sim t^{-2}$ for $t \to \infty$. Finally, for $t \to \infty$ and $i \to \infty$, the distribution function can be written in a self-similar way as (figure 4)

$$c(i, t) \approx \frac{1}{i^2} \left(\frac{i}{\langle i(t) \rangle} \right)^2 \exp\left(\frac{-2i}{\langle i(t) \rangle} \right). \tag{36}$$

Sum kernel $K_a(j, i) = j + i$. Similarly to the above case, the distribution function for the kernel

$$K_a(j, i) = j + i \tag{37}$$

is given by [18]

$$c(i, t) = \frac{i^{i-1} \cdot \exp(-i)}{i!} (1 - \exp(-t))^{i-1} \cdot \exp(i \cdot \exp(-t)) \cdot \exp(-t) \tag{38}$$

(figure 3d), and the temporal behaviour of the mean aggregate is

$$\langle i(t) \rangle = M_2(0) \cdot \exp(2M_1 t). \tag{39}$$

With $M_1 = 1$ and $M_2(0) = 1$, this becomes

$$\langle i(t) \rangle = \exp(2t). \tag{40}$$

This means that the mean mass increases exponentially with time. This result is also in agreement with the earlier approximation, equation 23 with $\kappa = 1$, $c = 0$ and $\tau_c = 1/2$ for monodisperse growth† (figure 2).

As for the constant kernel, one can rewrite equation 38 for $t \to \infty$ and $i \to \infty$

$$c(i, t) \approx \frac{1}{i^2} \left(\frac{i}{\langle i(t) \rangle} \right)^{1/2} \exp\left(\frac{-bi}{\langle i(t) \rangle} \right), \tag{41}$$

with $b = $ constant (see figure 4).

Product kernel $K_a(j, i) = j \cdot i$. The concentration function for the product kernel

$$K_a(j, i) = j \cdot i \tag{42}$$

with monodisperse initial conditions has the form for $t < 1$ [19]

$$c(i, t) = \frac{i^{i-2}}{i!} \exp(-it) \cdot t^{i-1} \tag{43}$$

(figure 3g). The mean agglomerate mass is

$$\langle i(t) \rangle = \frac{M_2(0)}{1 - M_2(0) \cdot t}, \tag{44}$$

and with $M_2(0) = 1$

$$\langle i(t) \rangle = \frac{1}{1 - t}. \tag{45}$$

In that case, the situation is different to the cases of constant and sum kernels, as the mean mass diverges for a finite time t_g (in this case $t_g = 1$). This point is termed 'gelation'. Although the assumption of monodispersity in that case is not given, the earlier analysis comes to the same formal result if one uses equation 22 with $\kappa = 2$, $c = -1$ and $\tau_c = 1$ (figure 2).

General cases. In addition to these three widely known cases, general solutions are also known for the linear kernel $K_a(j, i) = A + B(j + i)$, with $A = $ const. and $B = $ const. [20, 21] and for the branched kernel $K_a(j, i) = (A + Bj) \cdot (A + Bi)$, with $A = $ const. and $B = $ const. [20, 22].

In general, the mean cluster mass $\langle i \rangle$ has the following asymptotic behaviour: in the case of non-gelling systems, i.e. for $\kappa < 1$, one gets

$$\langle i \rangle \propto t^{1/(1-\kappa)} \quad \text{for } t \to \infty, \tag{46}$$

and for gelling systems, i.e. for $\kappa > 1$, one gets

$$\langle i \rangle \propto \frac{1}{(t_g - t)^{1/(\kappa-1)}} \quad \text{for } t \to t_g. \tag{47}$$

---

†The difference between $\tau_c = 1/2$ (equation 40) and $\tau_c = 1$ (equation 35) depends on the use of the kernel $i + j = 2i$ for $i = j$. The factor 2 directly enters into the denominator of the timescale (see equation 20).

The transition between both stages occurs at $\kappa = 1$, for which the asymptotic mean agglomerate mass is

$$\langle i \rangle \propto \exp(gt^b) \qquad \text{for } t \to \infty, \tag{48}$$

in which the constants g and b depend on the details of the kernel.

Scaling behaviour. Considering the scaling behaviour of the kernel in the rate equation, one can get some additional interesting insight into the growth kinetics of dust aggregates [12]. Assuming a homogeneous kernel for large aggregates with $i, j \gg 1$,

$$K_a(ai, aj) = a^\kappa K_a(i, j), \tag{49}$$

and also for the interaction of large clusters with small clusters, i.e. for $j \gg i$,

$$K_a(i, j) \propto i^\mu j^\nu, \tag{50}$$

with

$$\kappa = \mu + \nu, \tag{51}$$

one can distinguish three classes of reactions: $\mu > 0$ (class I), $\mu = 0$ (class II) and $\mu < 0$ (class III). Due to geometric arguments, the parameters κ and ν are restricted to $\kappa \leq 2$ and $\nu \leq 1$. In class I, large aggregates are more reactive than small ones, while for class III small aggregates dominate the reaction rates. For class II, the reactivity of large and small aggregates is very similar. The class I and class III reactions will be reconsidered in section 3.1 where the implications for the aggregate structures will be discussed. For $\kappa \leq 1$, the systems are non-gelling, while gelling occurs for $\kappa > 1$.

For $\kappa > 1$, the stage for $t \gtrsim t_g$ is also termed 'runaway growth' in the astrophysical literature, because a few dust aggregates grow much faster than the remainder of the aggregates in the system, i.e. they 'run away' in size. There is no self-similar solution to the rate equation for $t \geq t_g$. Lee [23] suggested that there are two types of runaway growth that belong to the parameter ranges $\mu \leq 1$ and $\mu > 1$, respectively. In the former case, runaway growth starts at $t \approx t_g$, while in the latter case $t_g/\tau_c \to 0$, with τ_c according to equation 20.

As was shown in equations 36 and 41 that the concentration function can have self-similar solutions. In general, one can write [24]

$$c(i, t) \approx \langle i(t) \rangle^{-y} \; \Phi(x), \tag{52}$$

where $\Phi(x)$ is a universal function independent of the initial conditions and the variable x is given by the ratio of the agglomerate mass to the mean mass at time t, i.e. $x = i/\langle i(t) \rangle$. For mass-conserving systems, the exponent is $y = 2$.

When a self-similar solution exists, the mean aggregate mass $\langle i(t) \rangle$ needs to grow monotonically and is required to be bound, i.e. gelation must not occur. As the self-similar mass distribution is only reached after some time, equation 52 is only valid for $i, t \to \infty$ with the ratio $i/\langle i(t) \rangle$ being constant. It was shown above that for the constant kernel $K_a(i, j) = 1$, one gets $\Phi(x) \sim \exp(-x)$ and for $K_a(i, j) = i + j$, one gets $\Phi(x) \sim x^{-3/2} \exp(-x)$. For $K_a(i, j) = ij$, it was shown that for $t < t_g$ the scaling function is given by $\Phi(x) \sim x^{-5/2} \exp(-x)$.

For the sake of completeness, it should be mentioned that, in addition to the three kernels shown above, the existence of self-similar solutions of the mass distribution function was shown by Krivitsky [25] for the homogeneous kernels $K_a(i,j) = (i+j)^\kappa (\kappa = \in (0,1])$ and $K_a(i,j) = (i \cdot j)^{\kappa/2}$ $(\kappa = \in (0,2])$ and by Fournier and Laurençot [26] for the kernels $K_a(i,j) = (i^\mu + j^\mu)(i^{-\nu} + j^{-\nu})$ $(\mu \in [0,1),$ $\nu \in (0,\infty),$ $\kappa = \mu - \nu \in (-\infty,1)),$ $K_a(i,j) = (i^\mu + j^\mu)^\nu$ $(\mu \in [0,\infty), \nu \in (0,\infty), \kappa = \mu\nu \in [0,1))$ and $K_a(i,j) = i^\mu j^\nu + i^\nu j^\mu$ $(\mu \in (0,1), \nu \in (0,1), \kappa = \mu + \nu \in [0,1))$. The kernel $K_a(i,j) = (i^\mu + j^\mu)^\nu$ can be used to describe agglomeration due to ballistic collisions of dust agglomerates with the fractal dimension $D_f \geq 2$ with constant collision velocity. In that case, one gets $K_a(i,j) = (i^{1/D_f} + j^{1/D_f})^2$, i.e. $\mu = 1/D_f$, $\nu = 2$ and $\kappa = 2/D_f$. The kernel $K_a(i,j) = i^\mu j^\nu + i^\nu j^\mu$ was also discussed by Lee [27] who numerically treated all cases for $\kappa < 1$ and $\kappa > 1$. Unfortunately, analytical formulae for the self-similar solutions are not known.

For arbitrary homogeneous kernels, the self-preserving mass distribution can only be derived numerically. General analytic expressions exist only for the limiting cases $x \ll 1$ and $x \gg 1$ [12]. For large x, the scaling function has the general form

$$\Phi(x) \sim x^{-\kappa} \exp(-x) \quad \text{for } x \to \infty. \tag{53}$$

For small x, it must be distinguished between class I and class III systems. For non-gelling class III systems, the scaling function is given by

$$\Phi(x) \sim x^{-\tau} \exp(-x^{-|\mu|}) \quad \text{for } x \to 0, \tag{54}$$

where τ depends on the reaction kernel. For non-gelling class I systems, the scaling function becomes [12]

$$\Phi(x) \sim x^{-(\kappa+1)} \quad \text{for } x \to 0. \tag{55}$$

The mass spectra for class III are typically bell-shaped, whereas for class I systems, the mass spectra decrease monotonically from small to large masses.

Self-similar solutions do not exclusively exist for the pure coagulation equation but also for systems in which coagulation and fragmentation occur. Escobedo *et al.* [28] derive that stationary solutions to the rate equation also exist when coagulation is dominating for small grains whereas fragmentation dominates for large aggregates.

2.2.3. Polydisperse systems without mass conservation. In nature, many physical systems cannot be treated as perfectly isolated from their environments. Particle losses and/or particle gains are ubiquitous, particularly in astrophysics and atmospheric sciences, where dust grains might evaporate or condense, grow or shrink in size due to a non-equilibrium with the ambient gas. In addition to that, particle infall or accretion onto objects outside the considered system might act as mass sources or sinks. Therefore, solutions to Smoluchowski's equation which do not obey mass conservation will be briefly discussed.

Based on the earlier result by Dubovskii *et al.* [29] who showed that a steady state solution, i.e. $(\partial nm, t)/\partial t = 0$, to Smoluchowski's equation (equation 4) is given by

$$n(m) = \frac{\text{const.}}{T(m)} \tag{56}$$

for kernels with the form

$$K_{\mathrm{a}}(\bar{m}, m) = \frac{T(\bar{m})T(m)}{(m + \bar{m})^3} \qquad (57)$$

for an arbitrary function $T(m)$, Simons [30] showed that an even more general steady-state solution of the form

$$n(m) = \frac{Bm^{\psi}}{T(m)} \qquad (58)$$

exists for kernels with the form

$$K_{\mathrm{a}}(\bar{m}, m) = T(\bar{m})T(m)Q(\bar{m}, m) \qquad (59)$$

for an arbitrary function $T(m)$ and an arbitrary homogeneous function $Q(\bar{m}, m)$ with $Q(\varsigma\bar{m}, \varsigma m) = \varsigma^{\upsilon}Q(\bar{m}, m)$. The parameters υ and ψ are connected by $\psi = -(\upsilon + 3)/2$. It is clear that for a closed system of coagulating particles, no steady state solution to equation 4 exists. Therefore, the solutions equations 56 and 58 can only be valid for open systems, i.e. for systems with a source of particles of mass $m = 0$ [30]. Power-law mass distributions as candidates for asymptotic solutions to the growth equation including fragmentation were treated by Bishop and Searle [31].

2.2.4. Numerical solutions to Smoluchowski's equation. From the considerations of the previous paragraphs it is clear that the analytical solutions to Smoluchowski's equation represent only a tiny section of the possible solutions with only limited direct applications to agglomeration problems occurring in nature and in the laboratory. Numerous publications deal with the numerical treatment of the growth equation. In the astrophysical and planetary-sciences literature, these comprise, among many others, the papers by Ohtsuki *et al.* [32], Inaba *et al.* [33], Lee [23], Malyshkin and Goodman [34] and Goldreich *et al.* [35]. Of particular importance for the applications in planet formation is that the mass increase of the growing objects is considerable so that no linear mass grid can be used. Logarithmic mass bins bear the difficulty that they can exhibit severe numerical artifacts. Ohtsuki *et al.* [32] find that the bin size should be smaller than $\sqrt{2}$.

2.3. *Non-isotropic systems*

The description of dust agglomeration becomes more complex when the system in which agglomeration takes place shows spatially asymmetric behaviour, e.g. from the influence of long-range directional forces. There are a number of experimental and theoretical studies of the effect of long-range forces on the aggregation behaviour [36–40] which will not be discussed. However, a few recent examples of non-isotropic systems will be presented.

2.3.1. Alignment of dust aggregates by gas drag in systems with external force. Blum and Wurm [41] produced fractal dust aggregates with $D_{\mathrm{f}} \approx 1.9$ and introduced the aggregates in an environment of rarefied gas (pressure $\sim 100\,\mathrm{Pa}$). They observed that the dust aggregates settled to the ground due to gravity at constant velocity. However, the spatial orientation of the fractal

aggregates, given by the direction of the longest axis with respect to the gravitational vector, was not random. Fractal aggregates typically have some arbitrary elongation that amounts to about a factor of two for the dust aggregates used by Blum and Wurm. During the sedimentation, it was observed that the aggregates were predominantly aligned such that their longest axis tended to be more parallel to the sedimentation velocity vector. Thus, the collision cross section in a system of differentially settling fractal dust aggregates will be slightly smaller than if the aggregates were oriented randomly. In addition to that, the sedimentation velocities of the aggregates, and, thus, also the collision velocities between the aggregates, if no other source of relative velocity is present, depend on the orientation of the grains (see equation 85 in section 3 for a formal treatment of the gas–aggregate friction time τ_f, from which the sedimentation velocity in free molecular flow can be derived by $v_s = g\tau_f$).

2.3.2. Alignment of dust aggregates and enhanced agglomeration by magnetic force. If the dust aggregates are ferromagnetic and/or are exposed to external magnetic fields, the aggregation scenario is not easily describable by rate equations [42–46]. Similar to the case above, the collision cross sections are orientation-dependent if grain alignment by magnetic fields is present. In addition to that, ferromagnetic aggregates are the origins of a magnetic force field that determines the interaction of the aggregate with its neighbours. The force field is dependent on the distance between two aggregates and on their individual magnetization which makes a description by Smoluchowski's equation a complex task. Moreover, the strength of the bonds between the monomer grains within an aggregate will also be different to those in non-magnetic aggregates (see section 5.2). Nuth *et al.* [42] describe the formation of 'spiderweb' and 'net' morphologies, i.e. very open-structured aggregates, in an experiment with magnetic iron dust grains. The formation timescales of the aggregates are so short that aggregates with large monomer numbers form in the laboratory, whereas previous experiments with non-magnetic particles never showed aggregation. This means that, due to the long-range magnetic forces, the aggregation times are considerably shortened, demanding a strongly modified kernel in the rate equation. In the numerical simulations by Nübold and Glassmeier [44] and Dominik and Nübold [45] the interaction between magnetic dipolar dust particles was investigated. Due to the long-range magnetic forces between the grains, their collision cross section is enhanced by up to several orders of magnitude, depending on the relative velocities between the particles. Thus, aggregation proceeds much faster than for non-magnetic dust grains. In addition to that, the growth exponent $(1/(1-\kappa)$ in equation 46) was found to be 3.2 instead of ~ 1.7 for non-magnetic grains and growth driven by Brownian motion [47] (see section 4). The theoretical and numerical considerations of Dominik and Nübold [44, 45] show that the resulting aggregates have predominantly chain-like morphologies with very low fractal dimensions. In an experimental work, Nübold *et al.* [46] confirmed these theoretical results. They dispersed a cloud of magnetic particles and observed the aggregation of the dust grains by long-distance microscopy. Analysis of the video images and of scanning electron microscope (SEM) images of sampled dust aggregates showed that the aggregate morphologies ranged from

chain-like structures with $D_f \approx 1.2$ to web-like structures with $D_f \approx 1.5$. The experimental growth exponent was determined to be 2.7, much larger than the measured exponent of 1.7 [47] for Brownian-motion-driven aggregation of non-magnetic grains.

2.3.3. Alignment of dust aggregates and enhanced agglomeration by electrostatic force.

Based upon an observation of rapid aggregation of charged particles in an experiment on the International Space Station, Ivlev *et al.* [48] studied the influence of charged particles on the aggregation behaviour of dust. For the consideration of electrostatic (charge–charge and charge–dipole) forces, Smoluchowski's equation (equation 4) has to be replaced by

$$\frac{\partial n(m, Q, t)}{\partial t} = \frac{1}{2} \int_0^m \int_{-\infty}^{\infty} K_a(\bar{m}, \bar{Q}, m - \bar{m}, Q - \bar{Q}) n(\bar{m}, \bar{Q}, t)$$

$$\times \, n(m - \bar{m}, Q - \bar{Q}, t) \mathrm{d}\bar{Q} \mathrm{d}\bar{m} \tag{60}$$

$$- n(m, Q, t) \int_0^{\infty} \int_{-\infty}^{\infty} K_a(\bar{m}, \bar{Q}, m, Q) n(\bar{m}, \bar{Q}, t) \mathrm{d}\bar{Q} \mathrm{d}\bar{m},$$

where $n(m, Q, t)\mathrm{d}m\mathrm{d}Q$ denotes the number density of aggregates with masses in the range $m \ldots m + \mathrm{d}m$ and charges in the range $Q \ldots Q + \mathrm{d}Q$. It should be noted that equation (60) conserves mass and charge of the particulate system. If the particles are embedded in a plasma, equation (60) is not applicable due to the presence of electron and ion currents. The kernel $K_a(\bar{m}, \bar{Q}, m, Q)$ can still be expressed by the ansatz according to equation 10 for ballistic collisions. The influence of the electrostatic charges is included in a change of the collision cross section. Ivlev *et al.* [48] distin-guish between charge–charge (index ch) and charge–dipole (index d) interactions. The collision cross section between two dust particles with radii s_1 and s_2 for the two cases are then

$$\sigma_{\mathrm{ch}} = \pi(s_1 + s_2)^2 \cdot \left(1 - \frac{E_{\mathrm{ch}}}{E_{\mathrm{kin}}}\right) \tag{61}$$

and

$$\sigma_{\mathrm{d}} = \pi(s_1 + s_2)^2 \cdot \begin{cases} 2\sqrt{\dfrac{E_{\mathrm{d}}}{E_{\mathrm{kin}}}} & \text{for } \dfrac{E_{\mathrm{d}}}{E_{\mathrm{kin}}} > 1 \\ \left(1 + \dfrac{E_{\mathrm{d}}}{E_{\mathrm{kin}}}\right) & \text{for } \dfrac{E_{\mathrm{d}}}{E_{\mathrm{kin}}} < 1 \end{cases}. \tag{62}$$

Here, the electrostatic energies for the charge–charge, E_{ch}, and charge–dipole, E_{d}, interactions at contact and the kinetic energy, E_{kin}, are given by

$$E_{\mathrm{ch}} = \frac{1}{4\pi\epsilon_0} \frac{Q_1 Q_2}{(s_1 + s_2)}, \tag{63}$$

$$E_{\mathrm{d}} = \frac{\alpha_{\mathrm{d}}}{4\pi\epsilon_0} \frac{s_1^3 Q_2^2 + s_2^3 Q_1^2}{(s_1 + s_2)^4}, \tag{64}$$

and

$$E_{\text{kin}} = \frac{1}{2}\mu'v^2, \tag{65}$$

with Q_1, Q_2, ϵ_0, $\alpha_{\text{d}} = (\epsilon - 1)/(\epsilon + 2)$, μ', and v being, respectively, the charges on particles 1 and 2, the dielectric constant, a coefficient given by the dielectric permittivity ϵ of the like materials (see also section 6.3 for a comparison to optical properties), the reduced mass, given by the individual masses m_1 and m_2 of the two dust particles through $\mu' = m_1 m_2/(m_1 + m_2)$, and the relative velocity between the two grains. As can be seen by the occurrence of the kinetic energy, it is assumed that the overall motion of the particles is determined by kinetics as long as the dust grains are widely separated. When they get closer, their motion is assumed to be ballistic and influenced by electrostatic forces. For weakly charged dust grains, the electrostatic interaction energy at contact for the charge–dipole interaction is in most cases larger than that for the charge–charge interaction, i.e. $|E_{\text{d}}| > |E_{\text{ch}}|$ [48]. By analyzing the moment equations, Ivlev *et al.* [48] concluded that for heavily-charged particles, the mean mass of the system does not grow faster than linearly with time, i.e. even slower than in the non-charged case for Brownian motion (see equation 25 in section 2.2.1 and section 4). However, if the particles are weakly charged, the growth exponent (see section 2.1) must be replaced by $\kappa + \zeta/2$ when the agglomeration kernel has the form

$$K_{\text{a}}(\bar{m}, \bar{Q}, m, Q) \propto m_1^{\mu} m_2^{\nu} |Q_2|^{\zeta} + m_2^{\mu} m_1^{\nu} |Q_1|^{\zeta} \tag{66}$$

and $\kappa = \mu + \nu$. Ivlev *et al.* showed that gelation (runaway growth) occurs for $\kappa + \zeta/2 > 1$, in contrast to $\kappa > 1$ for the non-charged case. For fractal aggregates, runaway growth occurs for $D_{\text{f}} < 2$ when $\zeta = 2$ and for $D_{\text{f}} < 3/2$ when $\zeta = 1$ [48].

Although the interaction between a charge and an induced dipole is isotropic for a homogeneous particle, alignment of the dust aggregates due to static dipoles can occur when the charge distribution over the dust aggregate is inhomogeneous. In that case, the dipole will experience a torque in the electric field of the charged particle in addition to the attractive force in its inhomogeneous electric field. Thus, it is expected that, similar to the case with magnetic particles, elongated structures will evolve. This matches the findings by Ivlev *et al.* [48] and the findings by Marshall *et al.* [49] who also observed the rapid formation of elongated aggregates in a microgravity experiment.

Most 'realistic' systems will show a more or less pronounced deviation from perfect symmetry so that the before-mentioned examples give some guidelines for the studies of the particular system of interest. Unfortunately, there is no fixed recipe how to proceed with a dust-aggregation problem with non-isotropic systems. In addition to that, the generalized Smoluchowski equation (equation 60) is not applicable to all systems in which ion and electron currents are non-negligible, e.g. in dusty plasmas, because then the charge conservation on the dust particles is not guaranteed.

3. Agglomerate structures and their influence on dust aggregation

As was shown in the previous section, the physical interactions within an ensemble of dust particles are contained in the kernel of Smoluchowski's equation. Two limiting cases are interesting to consider. For astrophysical applications, collisions are mostly ballistic which means that the particle trajectories are linear over distances exceeding the dust particles' dimensions. In that case, the kernel is given by

$$K_{\mathrm{a}}(j, i) = \beta_{\mathrm{a}}(j, i; v) \; v(j, i) \; \sigma(j, i), \tag{67}$$

with $\beta_{\mathrm{a}}(j, i; v)$, $v(j, i)$ and $\sigma(j, i)$ being the sticking probability, the collision velocity and the cross section for collisions between agglomerates of monomer numbers i and j. For many cases in atmospheric sciences and for almost all applications in colloidal physics, the particle motion is diffusive even on short time and length scales. The kernel is then given by (see e.g. [1])

$$K_{\mathrm{a}}(j, i) = 4\pi \; (D(j) + D(i)) \; (s(j) + s(i)), \tag{68}$$

where $D(i)$ and $s(i)$ describe the diffusion constant and the size of an aggregate containing i monomer grains. It is obvious that all non-trivial factors in both kernels depend on the aggregates' masses. In this section, it will be considered how this mass dependence is affected by the aggregates' morphologies. It will be started with the fractal concept in dust aggregation (section 3.1) which will ultimately lead to a relation between aggregate mass and aggregate size. The utilization of this knowledge in Smoluchowski's equation will be provided in section 3.2. Section 3.3 will give an overview of the attempts for self-consistent treatment of dust aggregation.

3.1. *Description of agglomerate structures*

It will now be considered how the actual (symmetric) aggregation process affects the aggregate structures and how different aggregate structures can be modelled and described within the framework of a rate equation. Unfortunately, it is not possible to self-consistently determine the aggregate structures from a given aggregation process and the physical laws describing the interaction of the dust particles. Therefore one needs to make approximations and develop simplified models for the aggregate structures and then test whether the aggregate structures and the growth model are consistent with the physical situation.

Were the dust particles liquid, i.e. little droplets, their mass-size relation would be

$$m \propto s^3, \tag{69}$$

and two spheres would coalesce into one resulting sphere after a collision. Thus, returning to a discrete rate equation of the kind presented in equation 9 and to a reaction kernel of the type shown in equation 67 (i.e. for ballistic collisions), one can write for the collision cross section

$$\sigma(j, i) = \pi(s_{(j)} + s_{(i)})^2 \propto (j^{1/3} + i^{1/3})^2, \tag{70}$$

using the relation between the mass of a particle and the number of monomers given in equation 8. If the velocity field $v(j, i)$ among the particles and the sticking probability for a collision, $\beta_a(j, i; v)$ are known, Smoluchowski's equation can be solved numerically, resulting in a number-density function $n(i, t)$. However, due to the presence of *solid* dust particles, one cannot assume that the resulting dust agglomerate follows the mass-size relation given in equation 69. Therefore, it needs to be investigated what the possible agglomerate structures are and how they can be described in terms of a (modified) mass-size relation.

It is beyond today's computer capabilities to fully simulate the agglomeration of a complete ensemble of a large number of dust particles with molecular-dynamics techniques. Therefore, simplifications must be introduced to allow the deduction of approximate agglomerate structures. It was shown in the previous section that the mass distribution function $n(i, t) \cdot i^2(t)$ is either bell-shaped (class III; see, e.g., figures 3b and e), i.e. all agglomerates have similar masses, or increases monotonically towards smaller masses (class I; see, e.g., figure 3h), i.e. there are a few large and many small agglomerates. In both cases, however, the mean mass $\langle i(t) \rangle$ increases monotonically with time. Therefore, it is evident that the following two main approximations were developed:

(i) **Particle–Cluster Aggregation (PCA)**

In the PCA case, it is assumed that the aggregate, whose structure is to be determined, grows by the sequential accumulation of individual monomers (i.e. $i = 1$). As exclusively sticking collisions between large aggregates and small particles are considered, this case represents either class I reactions (see section 2) in which the small aggregates are less reactive and, thus, are not completely consumed in the aggregation process, or systems with a source of small particles. Thus, a prerequisite for the applicability of PCA is the occurrence of a broad size distribution which is always dominated by the number of small aggregates. In the simplest PCA simulations, the sequential aggregate masses are $i_{\text{PCA}} = 1, 2, 3, \ldots, n$.

(ii) **Cluster–Cluster Aggregation (CCA)**

In contrast to PCA, the assumption behind the CCA process is that at any time the mass spectrum of the aggregates is bell shaped. This means that the mean agglomerate mass and the mass of the agglomerate with the highest number density nearly coincide. This is due to the fact that the reactivity of smaller agglomerates is much higher so that they were quantitatively consumed in previous agglomeration stages. Thus, the preferential collision which contributes most to the mass gain of the agglomerates is between nearly equal-sized aggregates (see e.g. [9] for a real system). The simplest CCA process approximates this by assuming that collisions exclusively take place between aggregates of identical mass. As in each collision two equal-mass aggregates are combined, the aggregate masses in this CCA process follow the sequence $i_{\text{CCA}} = 1, 2, 4, 8, 16, \ldots, 2^n$. However, there are other recipes for the formation of CCA clusters that take into account the influence of the fractal aggregate structure on the aggregation kernel (see,

e.g. Smirnov [15]) so that CCA aggregates with masses different to 2^n can be formed.

In the context of dust aggregation in space and in the atmosphere, it is interesting to consider two distinct aggregate motions during the aggregation event:

(i) **Diffusive motion (Brownian motion)**
When dust aggregates are embedded in a gaseous medium and are in thermal equilibrium with this medium, they are subject to random impacts by the ambient gas molecules. This leads to the well-known effect of Brownian motion that was theoretically explained by Einstein [50]. If this diffusive motion leads to collisions among the dust aggregates and if the direction of motion of the aggregates changes over a distance that is much smaller than the size of the aggregates, the scenario under which aggregation occurs is termed diffusion-limited aggregation (DLA, see figure 5) [51]. Due to the diffusive motion of the dust in the vicinity of the collision partner with a small mean free path, the dust aggregates cannot penetrate deeply into one another (in contrast to the ballistic case, see below) so that the two dust particles/aggregates touch preferentially at their outer tips.

(ii) **Ballistic motion (linear motion)**
For many other sources of relative velocity between the dust particles/ aggregates (e.g. for gravitational force) or in the case that the mean free path of the Brownian motion exceeds the aggregate dimensions, the trajectories can be regarded as linear. This scenario is termed ballistic aggregation.

Historically, computer simulations on aggregation started with lattice models in which a particle was only allowed to occupy a lattice site. Later, more realistic off-lattice models were developed in which particles could travel on arbitrary trajectories. The ballistic models were pioneered by Vold [52, 53] and Sutherland [54], whereas the diffusion-limited models were developed by Witten and Sander [51, 55], Meakin [56–58] and others (see, e.g. [59]). A rather recent review on the properties of fractal particles was given by Smirnov [15]. Figure 6 shows examples of ballistic PCA and CCA aggregates. In general, the computer simulations consider at a given time a single aggregate to which either single particles (PCA) or an aggregate of similar mass (CCA) are added which travel either on ballistic or on diffusive trajectories with arbitrary impact parameter. As already mentioned in the previous section, the overall morphology of the aggregates can be described analogous to equation 13 by

$$ i = k \left(\frac{s}{s_0} \right)^{D_{\mathrm{f}}}, \tag{71} $$

where the scaling parameter k depends on the definition of the aggregate size s and on the fractal dimension D_{f}. However, the parameter k is usually of the order of unity (see [61] for a discussion of k). As the 'size' is not uniquely defined for an irregular-shaped agglomerate, a number of definitions of the aggregate size have been proposed, e.g. the radius of gyration, the hydrodynamic radius, the capture radius, or the radius which makes $k = 1$ when s is measured in units of the monomer
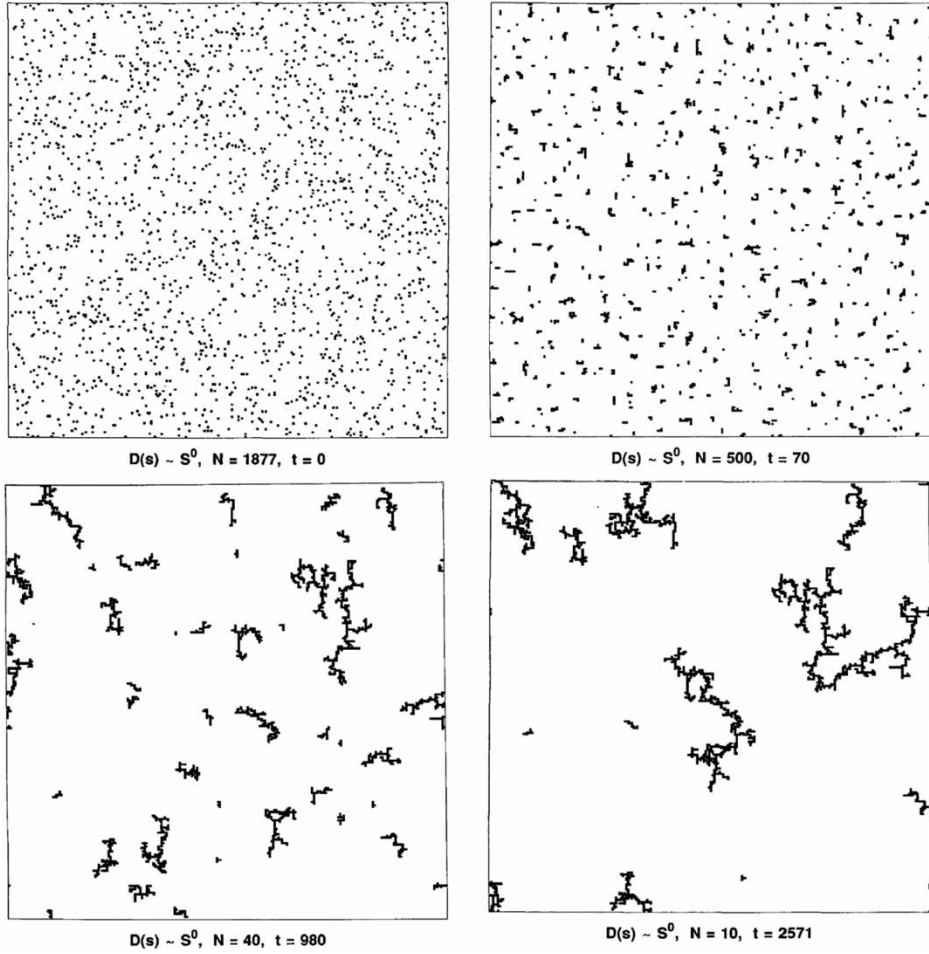
Figure 5. Diffusion-limited aggregation on a square lattice. Reproduced with kind permission [60]. © 1988 the American Physical Society. In this simulation, the diffusion constant is independent of the aggregate mass. Shown are the initial configuration (top left) and snapshots at $t = 70, 980, 2571$ (in arbitrary units).

radius s_0. However, the fractal dimension is rather independent of the definition of the aggregate size. Due to its applicability in modelling and experiment, here the radius of gyration s_g will be adopted as a measure for the aggregate size, which is defined by

$$s \equiv s_g = \left[\frac{1}{2N^2} \sum_{i=1}^{N} \sum_{j=1}^{N} (r_i - r_j)^2 \right]^{1/2}, \tag{72}$$

where the r_i and r_j give the three-dimensional position vectors of the N equal-mass constituent particles in the agglomerate. For aggregates with homogeneous internal

Figure 6. Examples of a three-dimensional ballistic cluster–cluster (left) and a three-dimensional ballistic particle–cluster (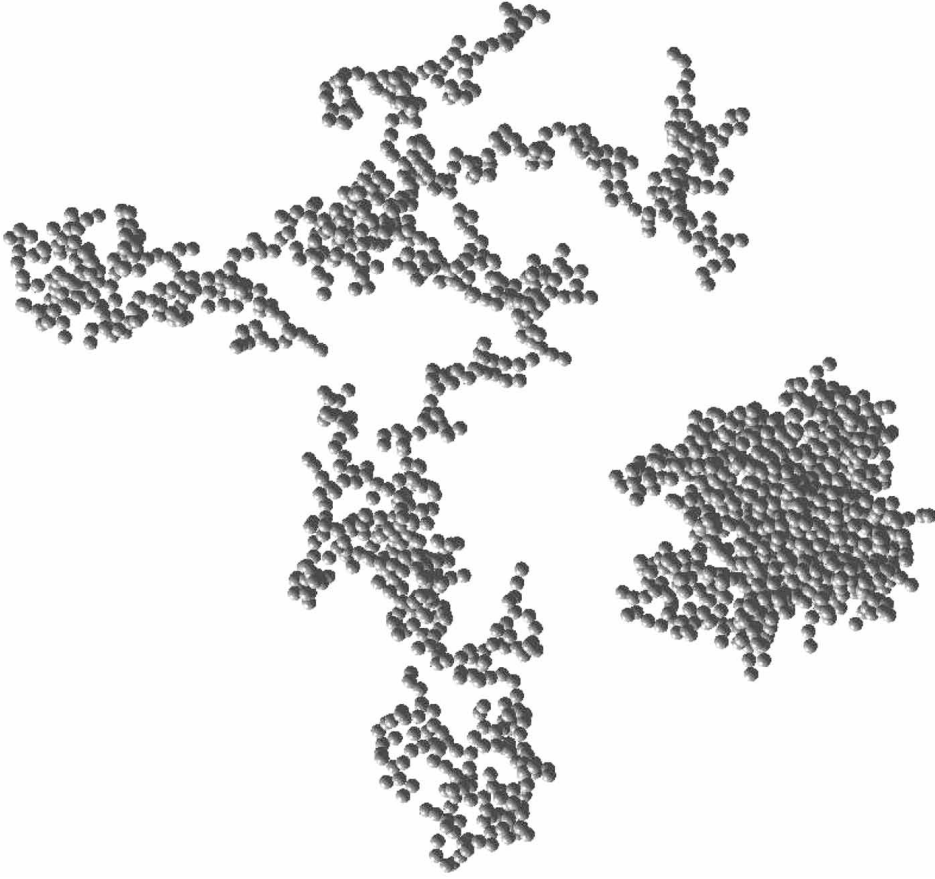right) aggregate. Both aggregates consist of $i = 1,024$ particles and are plotted to scale. The average fractal dimension of ballistic cluster–cluster aggregates is $D_f = 1.94$, ballistic particle–cluster aggregates have fractal dimensions of $D_f = 3$ (table 1).

particle density, e.g. for aggregates with $D_f = 3$, the radius of gyration is related to the aggregate radius s_a by $s_a = \sqrt{5/3}\, s_g$ [62].

Following the compilation by Smirnov [15], the four three-dimensional agglomeration models give the values for the fractal dimension shown in the centre column of table 1. Thus, the range of possible fractal dimensions for the simple models of dust aggregation is between $D_f \approx 1.8$ and $D_f = 3$.

A recent numerical simulation of the CCA process including thermal (Brownian) rotation of the dust aggregates showed that the rotational motion of the dust aggregates in the vicinity of the collision point is not negligible for the resulting aggregate structures [63]. The authors treated aggregate rotation during the approach of two equal-mass clusters explicitly and found an asymptotic value of $D_f = 1.46$ for low gas pressures. Thus, even for the 'thermal ballistic' case, the fractal dimension is

Table 1. The fractal dimensions for the four three-dimensional aggregation models relevant to this review. In the left data column, values are taken from the compilation by Smirnov [15]. The right column shows the results obtained by Paszun and Dominik [63]. N/A means that no data is available.

Aggregation process	D_f (excluding rotation)	D_f (including thermal rotation)
Ballistic PCA	3	N/A
Diffusion-limited PCA	2.46 ± 0.05	N/A
Ballistic CCA	1.94 ± 0.08	1.46
Diffusion-limited CCA	1.77 ± 0.03	< 1.46 (depending on gas pressure)

well below the value for ballistic CCA, $D_f = 1.94$. The fractal dimension is further diminished when the gas pressure is increased. Paszun and Dominik [63] did not investigate what the asymptotic value for very high gas pressures is. However, at their highest gas pressure, the fractal dimension of the aggregates was as low as $D_f = 1.11$. Due to the preferential collisions at their outer tips, the aggregates have much more elongated structures with less branching than for the non-rotation case.

All above-mentioned aggregation models assume that the aggregates collide in a hit-and-stick-like manner, i.e. the contact between the two colliding aggregates is frozen when they first touch. As will be shown later, this assumption is valid for very low collision velocities only (see section 5). At higher collision velocities, the single contact is no longer able to withstand the inertial forces and moments so that some aggregate restructuring occurs. A first approach to the treatment of aggregate structures including impact restructuring was made by Meakin and Jullien [64] and Jullien and Meakin [65]. In their numerical models, they assume a preservation of particle contacts (i.e. no breakage of particle–particle bonds). Upon first contact, the aggregates may 'fold', 'bend' and 'twist', depending on the number of allowed restructuring stages N_r ($N_r = 1$ for bending, $N_r = 2$ for bending and folding, and $N_r = 3$ for bending, folding and twisting). For CCA aggregates grown by DLA, the fractal dimension increases from $D_f = 1.80$ for $N_r = 0$ (no restructuring) to $D_f = 2.09$ for $N_r = 1$, $D_f = 2.17$ for $N_r = 2$ and $D_f = 2.18$ for $N_r = 3$. For ballistic CCA aggregates, the fractal dimension changes from $D_f = 1.95$ for $N_r = 0$ to $D_f = 2.13$ for $N_r = 1$, $D_f = 2.18$ for $N_r = 2$ and $D_f = 2.19$ for $N_r = 3$. It is obvious that the differences between ballistic and diffusion-limited aggregates become very small when a simple model of aggregate restructuring is considered. However, it should be noted that $D_f = 3$ is never reached when particle contacts are unbreakable (see section 5.3).

For the following discussion it is important to note that two fractal aggregates with fractal dimensions D_1 and D_2, which are on crossing trajectories with fractal dimensions D_w, will make contact (i.e. will not miss each other) if $D_1 + D_2 + D_w > 3$ [66]. As any trajectory fulfils the condition $D_w \geq 1$ (e.g. for a ballistic trajectory $D_w = 1$) and as all fractal dimensions are $D_1, D_2 \geq 1$ (table 1), this conditions is always fulfilled. Thus, one can conclude that the collision cross sections can be approximated by $\sigma \propto (s_1 + s_2)^2$, with s_1 and s_2 being the radii of the two

aggregates. A more detailed treatment of the collision cross sections will be given in section 3.2.2.

3.2. *Use of the aggregate structure in Smoluchowski's equation*

For the use of the results of the above-presented studies in a statistical treatment by Smoluchowski's equation (equation 9), knowledge of the reaction kernel is required. It will again be distinguished between diffusion-limited and ballistic conditions as they lead to different results.

3.2.1. Diffusive motion (Brownian motion).

The aggregation kernel for diffusion-limited aggregation is given by (see e.g. [1])

$$K_a(j, i) = 4\pi \, (D(j) + D(i)) \, (s(j) + s(i)), \tag{73}$$

where $D(i)$ and $s(i)$ describe the diffusion constant and the size of an aggregate containing i monomer grains†. Due to the low collision velocity of the grains, a sticking probability of unity can be assumed when the dust particles are not too large. The diffusion constant for spherical particles is given by

$$D = \frac{kT}{f}, \tag{74}$$

where k, T and f denote Boltzmann's constant, the gas temperature and the friction coefficient, respectively. For the two limiting cases of free molecular flow (very thin gas, in which the Knudsen number, the ratio between the mean free path of the gas molecules and the size of the dust aggregate is very large, i.e. $Kn = l_g/s \gg 1$) and viscous flow (very dense gas, $Kn \ll 1$), the friction coefficient of a spherical grain is given by

$$f = \frac{4}{3}(\delta P)\pi s^2 \rho_g \sqrt{\frac{8kT}{\pi m_g}} \tag{75}$$

(free molecular flow) and

$$f = 6\pi\mu_g s \tag{76}$$

(viscous flow), respectively, where s, m_g, ρ_g, μ_g and δP denote the radius of the spherical dust grain, the mass of a gas molecule, the mass density and the viscosity of the gas, and a coefficient describing the physical interaction of the gas molecules with the dust grain, respectively. The term $\sqrt{8kT/(\pi m_g)}$ in equation 75 is the mean velocity of the gas molecules. The coefficient (δP) is bound by $(\delta P) = 1$ for geometric reflection of the gas molecules and $(\delta P) = 1 + \pi/8 \approx 1.393$ for diffuse reflection. Hutchins *et al.* [67] found experimentally $(\delta P) = 1.30$. For the transition between the free molecular flow and the viscous regime, a correction to equation 76 of the form

$$f = \frac{6\pi\mu_g s}{C} \tag{77}$$

---

†For spherical particles, $s(i)$ and $s(j)$ are the particle radii in equation (73).

was introduced [68]. Here, the slip correction factor C is given by

$$C = 1 + \frac{l_g}{s}\left[A_1 + A_2\exp\left(-\frac{A_3 s}{l_g}\right)\right],$$ (78)

with l_g being the mean free path of the gas molecules. Kim *et al.* [69] review measurements of the parameters A_1, A_2, A_3 and present new measurements with monodisperse polystyrene latex (PSL) particles. While Davies [68] gives values of $A_1 = 1.257$, $A_2 = 0.400$, and $A_3 = 1.10$, more recent measurements with PSL particles by Hutchins *et al.* [67] yield $A_1 = 1.231$, $A_2 = 0.469$ and $A_3 = 1.178$. Kim *et al.* [69] get $A_1 = 1.165$, $A_2 = 0.483$ and $A_3 = 0.997$ for the range $0.5 \leq l_g/s \leq 83$.

It was experimentally shown by Blum *et al.* [70] that a relation equivalent to that in equation 75 can also be formulated for *dust aggregates* in the free molecular flow regime, when πs^2 is replaced by the geometric cross section of the aggregate. They found $(\delta P) = 1.11 \pm 0.17$ (95% confidence level) which is consistent with a theoretical value $(\delta P) = 1.24 \pm 0.01$ derived by Nakamura and Hidaka [71] for ballistic CCA agglomerates of $i = 1, \ldots 1000$, constituents. Krause and Blum [47] showed experimentally that the diffusion constant for fractal agglomerates is $D(i) \propto i^{-0.91}$. For dust aggregates in the viscous-flow regime the particle radius s should be replaced by the hydrodynamic radius s_h, for which an expression equivalent to that in equation 71 can be formulated, i.e. $i \propto s_h^{D_h}$, where D_h is the hydrodynamic fractal dimension (see, e.g. [15]). Wiltzius [72] showed experimentally that $s_h/s_g \approx 0.7$ for fractal aggregates consisting of nanometer-sized particles, where s_g is the radius of gyration of the aggregate (see equation 72). To a reasonable approximation, one can use $s_h \approx s_g$.

3.2.2. Ballistic motion (linear motion).

If the mean free path of the aggregates exceeds the aggregate size or if the aggregates are on linear trajectories, the collision kernel for the rate equation is given by (see equation 67)

$$K_a(j, i) = \beta_a(j, i; v)\, v(j, i)\, \sigma(j, i).$$ (79)

In the following, a relation between the masses of two arbitrary dust aggregates j and i and their pair-collision cross section $\sigma(j, i)$ will be sought. In the case of spherical and homogeneous particles this is given by equation 70. For fractal dust aggregates, an exact treatment for the problem of collision cross section is not available. If one assumes that the 'periphery' of an aggregate does not considerably contribute to the cross section, the radii of the two colliding aggregates with constituent numbers i and j are given by $s_i = s_0(i/k)^{1/D_f}$ and $s_j = s_0(j/k)^{1/D_f}$ (see equation 71). Based upon that, one can estimate the collision cross section to be approximately

$$\sigma(i, j) = \pi(s_i + s_j)^2 = \frac{\pi s_0^2}{k^{2/D_f}}(i^{1/D_f} + j^{1/D_f})^2.$$ (80)

Several other approximations for the collision cross section can be found in the literature [8, 15, 61]. Ormel *et al.* [73] have recently published a recipe for the determination of the extended volume of a dust aggregate. They introduced the *enlargement factor* Ψ, defined by

$$\Psi = \frac{V}{V^*},$$ (81)

where V and V^* denote the extended and the compact volume of the dust aggregate. For hit-and-stick collisions, like those assumed for ballistic particle-cluster and ballistic cluster-cluster aggregation (see section 3.1) or for low-velocity collisions among arbitrary dust aggregates (see section 5.3), they find that the enlargement factor of the resulting aggregate in a collision between two aggregates with masses m_1 and m_2 is given by

$$\Psi(m_1, m_2) = \langle\Psi\rangle_m \left(1 + \frac{m_2 \Psi_2}{m_1 \Psi_1}\right)^{(1/2)\delta - 1} + \Psi_{add}. \tag{82}$$

Here, $\langle\Psi\rangle_m = (m_1\Psi_1 + m_2\Psi_2)/(m_1 + m_2)$ is the mass-averaged enlargement factor, Ψ_{add} is a correction term for small aggregates, and δ is the exponent in the relation between mass and cross section, $A(m) \propto m^\delta$, with $2/3 \leq \delta \leq 1$. For aggregate–aggregate collisions in which the individual aggregate structures are not preserved (e.g., due to compaction, see section 5.3), Ormel *et al.* [73] derived for the enlargement factor

$$\Psi = (1 - f_c)(\langle\Psi\rangle_m - 1) , \tag{83}$$

with $f_c = E/(N E_{roll})$ and E, E_{roll} and N being the kinetic collision energy, the rolling-friction energy (see equation 111) and the total number of monomer grains in the two colliding aggregates. For the use in Smoluchowski's equation, one should keep in mind that the collision cross section is given by

$$\sigma(m_1, m_2) = \pi \left(\sqrt[3]{\frac{3 V_1^* \Psi_1}{4}} + \sqrt[3]{\frac{3 V_2^* \Psi_2}{4}}\right)^2 \tag{84}$$

and V_i and m_i are related through $m_i = \rho_i V_i$, with ρ_i being the mass density of the monomer material of aggregate i.

3.3. *Self-consistent treatment of agglomerate structures*

In the following, the problem of the self-consistent description of agglomerate structures and size distributions will be considered. Smoluchowski's equation does not provide for the derivation of agglomerate structures so that the afore-mentioned approximations by diffusion-limited and ballistic PCA and CCA were introduced. There are only a few studies in which a fully self-consistent treatment of the agglomeration problem was performed. One such study was published by Kempf *et al.* [74] in which the agglomeration of monodisperse, spherical particles due to Brownian motion in astrophysical environments was investigated. Initially, a virtual three-dimensional space was filled with N single particles. Kempf *et al.* [74] subdivided the random diffusive motion of the dust particles in pseudoballistic path segments in which possible collisions with neighbouring dust particles were searched for. After the detection of a collision, the two particles were joined to form a new dust aggregate. To account for thermal rotation, the new aggregate was then randomly rotated. In each time step, this was done for all detected collisions, whereupon in the next time step the process started anew. The resulting aggregate structures are consistent with the growth scenario by low-velocity Brownian motion (see section 5), because in each collision the exact contact point between two

aggregates was calculated and a hit-and-stick behaviour with a sticking probability of unity was assumed. Kempf *et al.* [74] adjusted the time steps to 1/50 of the smallest friction time in the ensemble. The friction time is given by [75]

$$\tau_f = \frac{m}{\sigma_a} \frac{1}{\rho_g \bar{v}}, \tag{85}$$

where m, σ_a, ρ_g and $\bar{v} = \sqrt{8kT/(\pi m_g)}$ are the mass and the aerodynamic cross section (i.e. the projected area) of the dust aggregate, the mass density of the gas and the mean thermal velocity of the gas molecules (see also equation 75), respectively. In contrast to earlier simulations in which the volume was kept constant, Kempf *et al.* [74] kept the number of dust aggregates within their volume approximately constant. Due to the aggregation process, the number of aggregates per volume decreases with time. Hence, the number of reactions per time step decreases considerably. To compensate for this, Kempf *et al.* [74] increased the volume accordingly and filled the added volume with arbitrarily chosen copies of the aggregates from the original volume. Kempf *et al.* [74] found in their simulations that the fractal dimension of the forming dust aggregates could not be described by a single value but followed a slightly asymmetric, bell-shaped distribution with a peak centered at $D_f^{(peak)} = 1.7$, a mean value of $D_f^{(mean)} = 1.8$ and a FWHM of $\Delta D_f = 0.5$. The mean value matches the fractal dimension found for diffusion-limited CCA (table 1) although the mean free path of the dust aggregates were exceeding their sizes which should result in ballistic collisions, i.e. in a fractal dimension of $D_f = 1.94$ (table 1). A distribution of fractal dimensions for Brownian agglomeration was also found by Kostoglou and Konstandopoulos [61] who used a Monte Carlo approach in the free-molecular flow and in the continuum regime. However, the width of the distribution function of the fractal dimension has a FWHM of $\Delta D_f \approx 0.02$ and, thus, is much narrower than that found by Kempf *et al.* [74].

In agreement with earlier simulations, Kempf *et al.* [74] found that in their simulations the aggregate mass distribution function developed into a self-similar shape that can be described by a bell-shaped scaling function similar to those described in section 2. As expected, the mean agglomerate mass follows a power law in time, i.e. $\langle i \rangle \propto t^z$, with $z = 1.9, \ldots, 1.3$, depending on the number density of the particles. This variation in the power law cannot be described by Smoluchowski's equation. The approach by the rate equation predicts for the scenario simulated by Kempf *et al.* [74] $z = 1.8$ which agrees to the numerical results when the number densities are low. For higher number densities, the exponent z decreases. Kempf *et al.* [74] explain this by a statistical effect that is not accounted for in Smoluchowski's equation: when the number of aggregates within a volume described by the collision length of the aggregates, i.e. the mean distance between two collisions, decreases, the available ensemble of collision partners for the aggregate can no longer be described by a mean-field theory such as the one used in Smoluchowski's equation. However, it seems that the deviation from the statistical rate equation in the simulations by Kempf *et al.* [74] is larger for higher number densities. This point still needs to be addressed in future work.

As a synthesis between sections 2 and 3, one can conclude that a number of numerical algorithms for the solution of Smoluchowski's equation with fractal

aggregates was developed. As an example, one recent and efficient algorithm which conserves the total mass of the aggregates and can also treat break-up of particles was developed by Kim and Kramer [76] and uses several different fragmentation kernels. The interested reader is referred to the original publication [76] and references therein.

4. Experimental verification of the applicability of Smoluchowski's equation for dust aggregation processes

So far, the theoretical aspects of dust aggregation and its mathematical description by Smoluchowski's equation and fractal dust aggregates have been considered. A recent experiment on Brownian motion driven dust aggregation offers for the first time the opportunity to compare the theoretical expectations with empirical results under rarefied-gas conditions relevant for astrophysical applications. This section serves both, an application of the methods developed in the preceding sections and a critical assessment of the general concept.

The picture one gets from the two previous sections is that for 'ideal' systems which consist of monodisperse spherical particles with a sticking probability of unity, without fragmentation, particle gain or loss, the rate equation (27) and the corresponding asymptotic solutions for the agglomerate mass (equations 46–48) are well-suited to describe the growth of aggregates as long as sufficient information concerning the reaction kernel is available. For the cases of interest, the kernels can either be described by ballistic (equation 79) or by diffusion-controlled collisions (equation 73). The relation between the collision cross section and the aggregate mass as well as between aggregate size and aggregate mass (equation 71) can be approximated by the assumption of fractal particles. When considering ballistic collisions, the relative velocities between the dust aggregates are given by the physical scenario under the assumption of fractal particles, involving the friction time (equation 85). In the case of diffusion-controlled aggregation, the diffusion constants can be derived by equations (74–78) for spherical particles in the free-molecular flow and the viscous flow limit and for fractal aggregates with $D_{\mathrm{f}} \approx 1.4$ in the transition regime by the relation $D(i) \propto i^{-0.91}$ [47].

The question is whether one can experimentally replicate such 'ideal' systems in which the descriptive parameters are fully available. Monodisperse spherical particles are commercially available in many different sizes and materials. They are often used as tracers in experiments involving fluid motion. An experimental difficulty is that one needs to find a system in which the initial condition of single particles and a sticking probability of unity for all collisions between the particles/aggregates can be realized. As will be shown in section 5, the sticking probability is a function of collision velocity and particle size so that low-velocity collision experiments with small dust particles are favourable. However, such small particles also tend to stick to one another so strongly before the experiments that the deagglomeration of the dust sample into single particles becomes increasingly difficult for smaller particle sizes. Moreover, for experiments involving agglomeration processes in dilute gas, e.g. for the simulation of astrophysical aggregation scenarios, the deagglomeration and subsequent dispersion of the dust sample is required for rarefied-gas conditions.

Blum *et al.* [77] and Poppe *et al.* [78] developed methods for the deagglomeration and dispersion of dust grains into rarefied gases. The methods either comprise the separation of the individual dust particles by contact with a fast-rotating mechanical device or by using the differential drag forces inside a rarefied-gas shock wave. All these methods work efficiently as long as the grain sizes are not much below 1 μm in diameter. Thus, the experiments described hereafter used particles with sizes of typically ~ 1 μm.

An experimental investigation in which the evolution of initially monodisperse samples of spherical SiO_2 particles was studied is described by Blum *et al.* and by Krause and Blum [47, 79, 80]. For the simulation of the initial growth stages of dust aggregates in the young solar system, they dispersed an ensemble of single spherical SiO_2 particles in a rarefied-gas atmosphere and observed the subsequent evolution of the dust grains using two-dimensional and three-dimensional long-distance-microscopy techniques. As in the early solar system, collisions between the dust grains were caused by Brownian motion. For small dust aggregates, individual collisions were ballistic; for large aggregates, collisions were dominated by the diffusive motion of the particles [70, 80–83]. Due to the low collision velocities of typically $v(j,i) \lesssim 10^{-3}$ ms^{-1}, the sticking probability can be very well approximated by $\beta_a(j,i;v) = 1$ (see sections 5.2 and 5.3). However, in the laboratory, gravitational sedimentation velocities exceed the relative grain velocities due to Brownian motion by much so that all experiments were performed under microgravity conditions in a space-shuttle and a sounding-rocket flight. The space-shuttle experiment used monodisperse spherical SiO_2 grains with a radius of 0.95 μm [80] while the monomers in the sounding-rocket experiment had 0.5 μm radius [47].

The results from both aggregation experiments show that the morphologies of the resulting dust aggregates can be described by equation (71) with a fractal dimension of $D_f = 1.41 \pm 0.06$ [47] (figure 7), in agreement with recent computer simulations by Paszun and Dominik [63]. The low fractal dimension results from the effect of Brownian rotation (table 1). The relation between the geometric cross section σ_g and the mass of the fractal aggregates is $\sigma_g \propto i^{0.9}$. Due to a lack of better data on collision cross sections of aggregates with arbitrary fractal dimensions $D_f < 2$, the collision cross section is approximated by the sum of the geometric cross sections of the two aggregates. Thus,

$$\sigma(i,j) \propto i^{0.9} + j^{0.9}. \tag{86}$$

The mean collision velocity of two aggregates with i and j constituents of individual mass m_0 can be described by

$$v(i,j) = \sqrt{\frac{8kT}{\pi m_0} \cdot \frac{i+j}{i \cdot j}} \propto \left(i^{-1} + j^{-1}\right)^{0.5}. \tag{87}$$

For ballistic collisions (i.e. for small agglomerates), the kernel should thus become

$$K_a(i,j) \propto (i^{0.9} + j^{0.9}) \cdot \left(i^{-1} + j^{-1}\right)^{0.5}. \tag{88}$$

The scaling of the collision kernel results in (see equations 49 and 50)

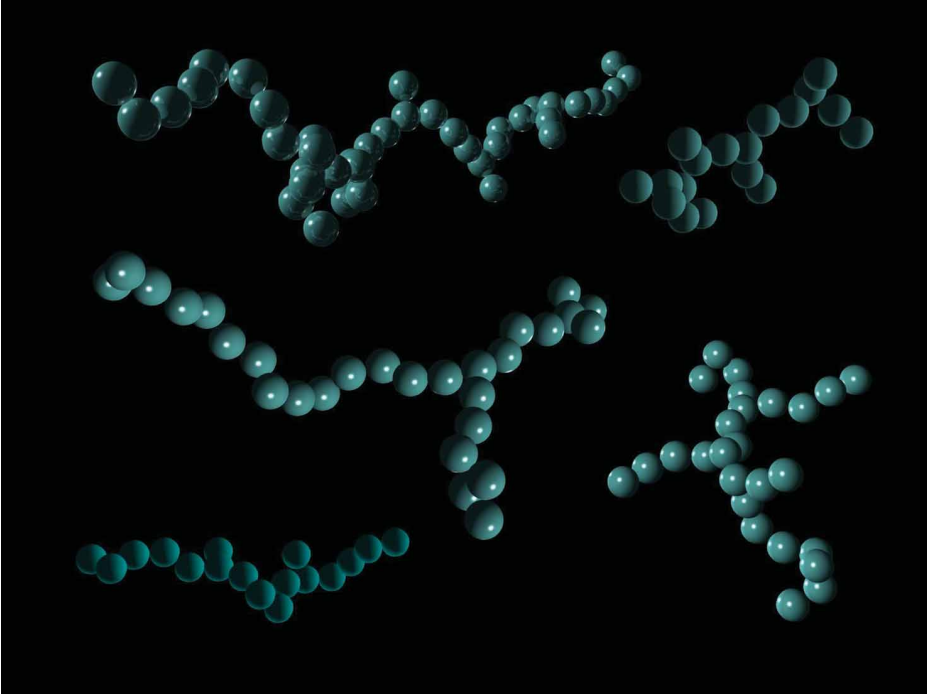$$K_a(ai, aj) = a^{0.4} K_a(i,j) \tag{89}$$

Figure 7. Reconstruction of dust aggregates consisting of monodisperse spherical particles from a microgravity experiment. The dust aggregates have a fractal dimension of $D_f = 1.41 \pm 0.06$ and were grown by Brownian motion-induced collisions [47, 80]. Reproduced with permission [47, 80]. © 2004, 1991 the American Physical Society.

and for $j \gg i$

$$K_a(i,j) \sim i^{-0.5} j^{0.9}. \tag{90}$$

Thus, the aggregation scenario is of class III (see section 2). As is typical for class III, the experiments show that the mass spectra are bell-shaped. Thus, the approximation $i \approx j$ (see section 2.2) can also be used here which results in the prediction

$$\langle i \rangle \propto t^{1/(1-0.4)} \approx t^{1.67}. \tag{92}$$

The experimental results are in agreement with a temporal growth exponent† of 1.71 ± 0.65 [47] (figure 8). However, for larger aggregates the collisions are no longer purely ballistic. In that case, the kernel is given by the product of the diffusivity and the aggregate size (see equation 73). As was already mentioned above, Krause and Blum showed that the diffusivity for fractal dust aggregates can be approximated by [47]

$$D(i) \propto i^{-0.91}. \tag{92}$$

---

†The error for the exponent is a formal result of an unconstrained three-parameter fit of the data points in figure 8 to a function given in equation 22. Constraining τ_c and c in equation 22 would result in a smaller error for the exponent.
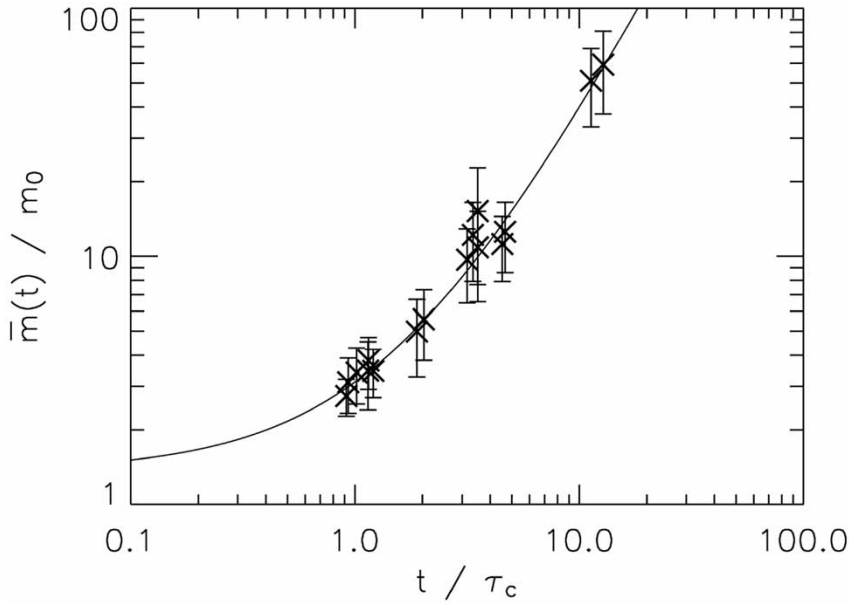
Figure 8.	Mean aggregate mass as a function of time (in units of the monomer collision time τ_c) for fractal dust aggregates and Brownian-motion-induced aggregation [47]. The solid line is an approximate growth model of the form of equation 22 with a growth exponent of 1.7.

Thus, the diffusive kernel for large dust aggregates is given by

$$K_a(i,j) \propto (i^{-0.91} + j^{-0.91}) \cdot (i^{1/D_f} + i^{1/D_f}). \tag{93}$$

With $D_f = 1.41$, the scaling of this kernel is

$$K_a(ai, aj) = a^{-0.20} K_a(i,j) \tag{94}$$

and for $j \gg i$

$$K_a(i,j) \sim i^{-0.91} j^{0.71}. \tag{95}$$

Thus, the diffusion-limited aggregation is also of class III, and one expects a temporal evolution of the mean aggregate mass

$$\langle i \rangle \propto t^{1/(1+0.2)} \approx t^{0.83}, \tag{96}$$

much weaker than in the ballistic case. It turns out that the mass spectra of the aggregates can help to reveal whether ballistic or diffusion-limited growth are dominating. Figure 9 shows the measured self-similar mass distribution function (squares) in comparison to solutions of Smoluchowski's equation with the kernels in equation 88 (shaded area in figure 9a) and 93 (shaded area in figure 9b). The shaded areas denote the one-standard-deviation range of possible solutions
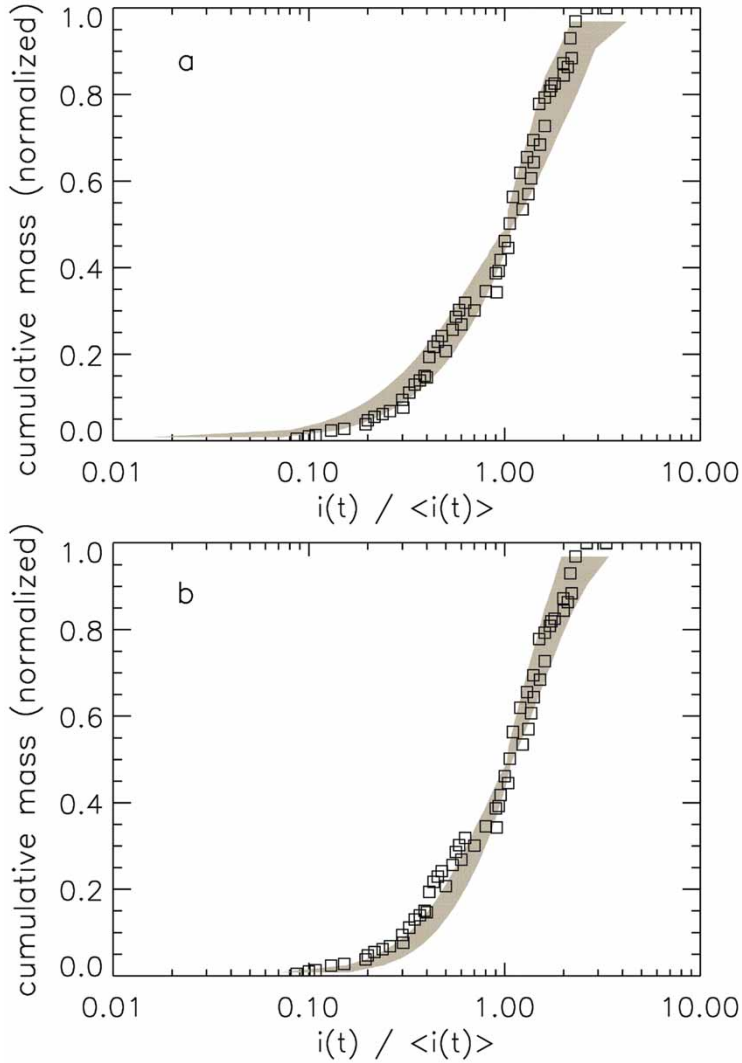
Figure 9. Self-similar cumulative mass spectrum of fractal dust aggregates formed by Brownian-motion-induced aggregation (squares) [47]. Reproduced with permission [47]. © 2004 the American Physical Society. For comparison, solutions to Smoluchowski's equation for ballistic (a) and diffusion-limited (b) aggregation are shown as shaded areas.

when 59 dust aggregates† are randomly drawn from the respective probability functions following from equations (88) and (93). With this method, a comparison between experiments and theoretical calculations is possible. It can be seen from figure 9 that the experimental mass spectrum falls in between the two limiting

---

†This is the same number of aggregates that was used for the generation of the experimental mass spectrum in figure 9.

cases. Thus, experiments can help to find the kernel for the complex transition regime between ballistic and diffusion-limited aggregation.

For Brownian agglomeration, the existence of a universal mass distribution function was predicted by Vemury and Pratsinis [84] and by Zurita–Gotor and Rosner [85]. A self-preserving size distribution was also found in the experiments by Friedlander and Hidy [86] who investigated the size distribution function of tobacco smoke and by Matsoukas and Friedlander [87] who observed the agglomeration of irregular-shaped metal-oxide particles in the free-molecular flow regime. However, neither experiment used monodisperse particles and mono-disperse initial conditions.

With this example it is shown that the statistical approach for the description of dust aggregation with fractal particles is valid and can be used for the description of the evolution of an ensemble of dust aggregates. However, it should again be noted that Smoluchowski's equation cannot predict the fractal nature of the dust aggregates nor the collision cross section of these grains. The latter can only be obtained experimentally or by realistic computer simulations of the respective aggregation processes.

Another example in which the concept of the growth equation was proven used monodisperse spherical SiO_2 grains of $0.95\,\mu m$ radius in a rarefied turbulent gas [9]. The absolute collision velocities in this experiment were $v(j, i) \leq 0.5\,ms^{-1}$ so that the assumption of perfect sticking is also valid (see sections 5.2 and 5.3). It turned out that for this aggregation scenario the aggregate structures can be nicely modelled by the ballistic CCA simulations, i.e., the aggregates have fractal dimensions of $D_f = 1.91$ (table 1). Thus, the collision cross sections for this case can be derived by the formalism given by Ossenkopf [8]. The relative velocity between two grains with masses i and j depends on the difference in friction time (see equation 85) and can be described by

$$v(i, j) \propto |\tau_f(i) - \tau_f(j)| \propto \left| \frac{i}{\sigma_a(i)} - \frac{j}{\sigma_a(j)} \right|, \tag{97}$$

where $\sigma_a(i)$ is the aerodynamic cross section of the aggregate of mass i in the free molecular flow regime. Wurm and Blum [9] showed that the shape of the mass spectra as well as their temporal evolution can be successfully modelled by Smoluchowski's equation. They also showed that the bell-shaped mass distribution functions lead on average to preferential collisions between the median-mass aggregate $\bar{i}$ and an aggregate whose mass is $\bar{j} \approx \bar{i}/2$. Thus, the assumption of quasi-monodispersity, which is a prerequisite for CCA, is very well justified.

5. The physics of dust agglomeration

So far, the *microphysics* involved in the dust-aggregation process has been neglected. In this section, a review of recent investigations on the physical interactions in particulate systems shall be given. It will start with the description of the dust–gas interaction (section 5.1) for arbitrary gas pressures. The knowl-edge of the dust–gas interaction is essential for the determination of the collision

velocities, grain alignment (see section 2.3.1) and the decision whether diffusive or ballistic motion is dominating (sections 3.1 and 3.2). In the subsequent subsection (section 5.2), the physics in grain–grain contacts and the causes for grain sticking in mutual collisions will be treated. Fractal dust aggregates can have very open structures which might get compacted in mutual collisions. This involves dynamical effects in grain–grain contacts, such as rolling and sliding. Section 5.3 will summarize the knowledge in this field. Finally, recent progress in the field of physical interactions of macroscopic, non-fractal dust aggregates will be reviewed (section 5.4). A description of the collisions of large dust aggregates by continuum parameters is desirable as the number of individual particle–particle contacts is too high for a numerical treatment of all contacts.

5.1. *The interaction of fractal dust aggregates with the ambient gas*

Before one can come to the 'aerodynamic' properties of dust aggregates, the treatment of the interaction between spherical particles and gases is helpful. The drag force that a spherical dust particle of radius s experiences in a gas with mass density ρ_g when it is moving at a relative velocity v with respect to the gas is given by

$$F_D = \begin{cases} \dfrac{1}{2} \pi \, C_D \, s^2 \, \rho_g \, v^2 & : \quad \text{for } l_g \ll s \\[2mm] \dfrac{4}{3} \pi \, s^2 \, \rho_g \, v \, \bar{v} & : \quad \text{for } l_g \gg s, \end{cases} \tag{98}$$

with l_g and $\bar{v} = \sqrt{8kT/(\pi m_g)}$ being the mean free path and the mean thermal velocity of the gas molecules (see also section 3.2). The drag coefficient C_D is given by

$$C_D = \begin{cases} 24 \, Re^{-1} & : \quad \text{for } Re < 1 \\[2mm] 24 \, Re^{-0.6} & : \quad \text{for } 1 < Re < 800 \\[2mm] 0.44 & : \quad \text{for } Re > 800, \end{cases} \tag{99}$$

with the Reynolds number given by

$$Re = \frac{2 \, s \, \rho_g \, v}{\mu_g}. \tag{100}$$

Here, μ_g is the viscosity of the gas. For $Re < 1$, one gets the well-known Stokes drag force, $F_D = 6\pi\mu_g\rho_g sv$, while the case $l_g \gg s$ is termed the Epstein regime. For many applications, the particle stopping time

$$\tau_f = \frac{m \, v}{F_D} \tag{101}$$

is convenient to use (see also equation 85). Here, m is the mass of the dust particle. For the Stokes and the Epstein regime one get

$$\tau_{\mathrm{f}} = \begin{cases} \dfrac{2}{9}\dfrac{\rho\, s^2}{\mu_{\mathrm{g}}} & : \quad l_{\mathrm{g}} \ll s \text{ and } Re < 1 \text{ (Stokes)} \\[2ex] \dfrac{\rho\, s}{\rho_{\mathrm{g}}\, \bar{v}} & : \quad l_{\mathrm{g}} \gg s \text{ (Epstein)}, \end{cases} \tag{102}$$

where ρ is the mass density of the dust particle.

As already mentioned, Wiltzius [72] showed that the hydrodynamic radius is close to the radius of gyration for dust aggregates of all fractal dimensions. Moreover, Blum *et al.* [70] showed experimentally that in the free-molecular flow regime the lower equation 102 is in principle also valid for dust aggregates and takes the form

$$\tau_{\mathrm{f}} = \epsilon_{\tau}\, \frac{m}{\sigma_{\mathrm{g}}}\, \frac{1}{\rho_{\mathrm{g}}\, \bar{v}}, \tag{103}$$

where σ_{g} and ϵ_{τ} are the geometric cross section of the dust aggregate and a correction factor. Blum *et al.* [70] found experimentally $\epsilon_{\tau} = (0.68 \pm 0.10)$, while Meakin *et al.* [88] theoretically derived $\epsilon_{\tau} = 0.58$.

5.2. *Collisions and contacts between individual dust particles*

In the previous sections, it was always assumed that upon contact two dust grains stick to each other. Now, the physics behind grain sticking will be considered. It will be assumed that the dust particles are spherical in shape with radii s_1 and s_2 and that they are electrically neutral and non-magnetic. In that case, two grains will always feel a short-range attraction due to induced-dipole forces, e.g. van der Waals interaction. Stochastically varying dipoles of single atoms inside the dust grain induce dipoles in neighbouring atoms and cause an attractive dipole–dipole force. For two surfaces in contact, the resulting macroscopic force is given by [89]

$$F_{\mathrm{vdw}} = -\frac{A_{\mathrm{H}}\, R}{6\, z_0^2}, \tag{104}$$

where A_{H} and $z_0 \approx 4 \cdot 10^{-10}$ m are the material-dependent Hamaker constant and the equilibrium distance between the two adjacent surfaces, respectively. The reduced radius R can be calculated from $R = s_1 s_2/(s_1 + s_2)$. The Hamaker constant is temperature dependent and can be related to the dielectric properties of the materials (see, e.g. [90]). Some Hamaker constants for the contacts of two identical materials are given in table 2.

In the contact of two spherical particles, this attractive force results in an elastic deformation leading to a flattening of the grains in the contact region. As the range of the van der Waals force is very short (of the order of z_0), the contact flattening enhances the region of contact and, thus, further strengthens the contact. An equilibrium is reached when the attractive force equals the elastic repulsion force.

Table 2.   Hamaker constants for the contact of two like
materials. Data are taken from Israelachvili [91].

Substance	$A_H 10^{-20}$ J
Water	3.7
Cyclohexane	5.2
Benzene	5.0
Polystyrene	6.5
Fused Quartz (SiO_2)	6.3
Alumina (Al_2O_3)	14
Iron Oxide (Fe_2O_3)	21
Rutile (TiO_2)	43
Metals (Au, Ag, Cu)	25–40

For small, hard particles with low surface forces, the equilibrium contact force is given by [92]

$$F_c = 4\pi\gamma R, \tag{105}$$

where γ denotes the specific surface energy of the particle material†. The meaning of equation 105 is that a force F_c is required to separate two grains in contact (thus, F_c is positive). The separation force is of particular importance for the determination of impact fragmentation of dust aggregates (see below). A few years ago, it became possible to measure the contact force between individual microscopically small spherical particles and, thus, to confirm the validity of equation 105. Heim *et al.* [93] used a modified atomic force microscope (AFM) following the technique described by Ducker *et al.* [94] to directly measure the separation force between pairs of SiO_2 spheres with radii between $s = 0.5\,\mu m$ and $s = 2.5\,\mu m$ and reduced radii in the range $R = 0.35, \ldots, 1.3\,\mu m$. They found a linear relation between the reduced radius and the pull-off force and deduced a specific surface energy of the particles of $\gamma = 0.014\,Jm^{-2}$ which is close to the bulk value of SiO_2. In addition to the AFM method [93], a variety of other measurement principles of interparticular forces for micrometer-sized dust grains of various compositions exists (see [95, 96]).

To derive the dynamical interactions between small dust particles, Poppe *et al.* [97] designed an experiment in which single, micrometer-sized dust grains impacted smooth targets at various velocities (in the range $0, \ldots, 100\,ms^{-1}$) under vacuum conditions. The single particles were deagglomerated and accelerated by a specifically designed apparatus based upon a fast-rotating cogwheel [78]. The impacts were observed by a long-distance microscope with a stroboscopic illumination. Poppe *et al.* [97] found for spherical projectiles a sharp transition

---

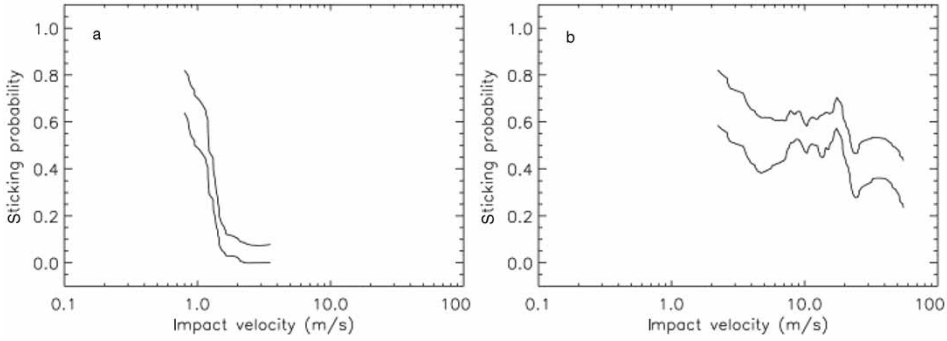†For further reading on equilibrium particle contacts, see [90].

Figure 10. Experimental determination of the sticking efficiency for micrometer-sized dust particles [97]. Figure 10a shows a typical example for spherical particles (here: SiO_2 particles with $s = 0.6\,\mu m$) hitting a flat surface target. Spherical particles exhibit a sharp threshold velocity for sticking. Irregular particles behave differently (see figure 10b as an example of irregular SiC particles with mean radii of $s = 0.3\,\mu m$); they have moderate sticking probabilities for a wide velocity range with a much wider transition from sticking to bouncing. In both cases, the targets consisted of flat, polished SiO_2. The two lines represent the 1-standard-deviation envelope of the experimental data.

from sticking with an efficiency of $\beta_a \approx 1$ to bouncing (i.e. a sticking efficiency of $\beta_a = 0$) (see figure 10). This threshold velocity is

$$
\begin{aligned}
v_s &\approx 1.2\,\mathrm{m s}^{-1} \quad \text{for } s = 0.6\,\mu m \\
v_s &\approx 1.9\,\mathrm{m s}^{-1} \quad \text{for } s = 0.25\,\mu m.
\end{aligned}
\tag{106}
$$

Thus, the threshold velocity for sticking increases with decreasing particle size. The target materials were either polished quartz or atomically smooth (surface-oxidized) silicon. A recent experiment by Reißaus *et al.* [2] showed that for nanometer-sized particles the sticking threshold increases to $v_s \gtrsim 1\,\mathrm{km s}^{-1}$ so that one can assume a roughly inverse proportionality between the threshold velocity for sticking and the particle size. Currently, there is no theoretical explanation available for the threshold velocity for sticking. Earlier attempts to model the low-velocity impact behaviour of spherical particles predicted much lower sticking velocities [98]. These models are based upon impact experiments with 'softer' polystyrene particles [99]. Although the sticking threshold velocities were similar to those found by Poppe *et al.* [97] for the harder silica spheres, the behaviour of the non-sticking grains was very different. In the experiments by Dahneke [99] (and also in those by Bridges *et al.* [100] using macroscopic ice particles), the coefficient of restitution which is defined by

$$
\epsilon_r = \frac{v_{\text{after}}}{v_{\text{before}}},
\tag{107}
$$

was always close to unity and increased monotonically with increasing impact velocity above the sticking threshold. Here, v_{before} and v_{after} denote the relative velocity of the grain to the target before and after the collision. In the experiments described by Poppe *et al.* [97] using 'hard', spherical SiO_2 particles, the average coefficient of restitution decreased considerably with increasing impact velocity

above the sticking threshold. In addition to that, Poppe *et al.* showed that the behaviour of an individual particle impact is not predictable due to a considerable scattering in individual values of the coefficient of restitution.

While spherical particles exhibit a sharp sticking threshold, the impact behaviour of irregular dust grains is more complex. Irregular particles of various sizes and compositions show an overall decrease in the sticking probability with increasing impact velocity. The transition from $\beta_a = 1$ to $\beta_a = 0$, however, is very broad (figure 10b) so that even impacts as fast as $v \approx 100 \, \mathrm{ms}^{-1}$ can lead to sticking.

An interesting side effect detected at these impact experiments is that all grains that do not stick after an impact carry away electrical charges from the target [101]. It turned out that the number of separated elementary charges in a collision between a dust particle with impact energy E_c can be expressed by [101, 102]

$$N_e \approx \left(\frac{E_c}{10^{-15}\mathrm{J}} \right)^{0.8}. \tag{108}$$

Impact charging can potentially lead to an enhanced sticking if a target agglomerate develops a surface charge whose electrical field can trap non-sticking particles in subsequent collisions [103].

5.3. *Collisions between fractal dust aggregates*

It was just shown that the collision between a pair of individual dust grains leads to sticking for low impact velocities, whereas for higher impact speeds the grains bounce off. How does this picture change when the collision is between two (fractal) dust aggregates? In addition to sticking and bouncing, a collision between two dust aggregates can potentially also lead to considerable deformation or even to (partial) destruction of the aggregates (figure 1). The first physical approach to the problem of aggregate–aggregate collisions was published by Dominik and Tielens [104] and was based upon an earlier work by the same authors [105]. In a numerical simulation, Dominik and Tielens [104] studied the interaction forces in a collision between two fractal dust aggregates. The aggregates consisted of equal-sized spherical particles, were of equal mass and shape and had an overall two-dimensional structure (i.e. the aggregates were flat). However, as the monomer particles were spherical (and not circular), the simulations can also be used for the prediction of collisions between dust aggregates in three-dimensional space. As interaction forces, Dominik and Tielens [104] explicitly treated adhesion as well as rolling and sliding between all pairs of grains in contact within the two colliding dust aggregates. The result of the numerical simulations is that there are, besides the total kinetic impact energy E_{im}, three decisive physical quantities which determine the outcome of the collision: (1) the number of grain–grain contacts within each of the two colliding aggregates, n_k, (2) the energy required to break a single grain–grain contact, E_{br} and (3) the rolling-friction energy, E_{roll}, required to roll two spherical monomer grains along a quarter of their circumference. Dominik and Tielens [104] found five energy regions in which the collision behaviour was distinguishable. Starting at the lowest impact velocities, aggregates behave in a hit-and-stick manner, i.e. the contact between the two first-touching monomers is established and frozen at

Table 3.   The outcomes of a collision between two equal-sized fractal dust aggregates
in the numerical simulations by Dominik and Tielens [104].

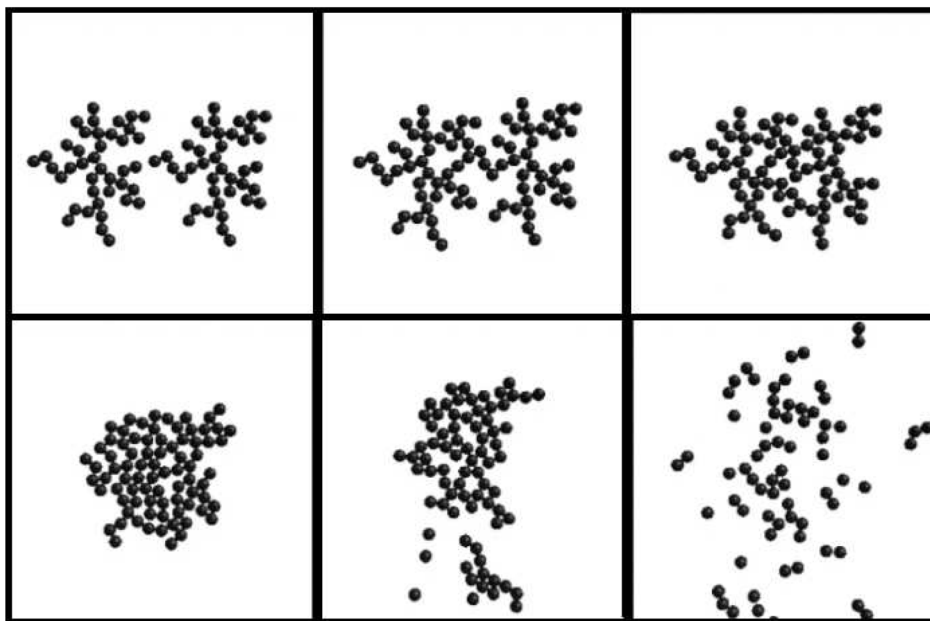| Case	Energy range	Outcome of collision
(1)	$E_{im} < 5 \cdot E_{roll}$	Hit-and-stick behaviour
(2)	$E_{im} \approx 5 \cdot E_{roll}$	First visible restructuring
(3)	$E_{im} \approx 1 \cdot n_k \cdot E_{roll}$	Maximum compaction
(4)	$E_{im} \approx 3 \cdot n_k \cdot E_{br}$	Loss of single monomer grains
(5)	$E_{im} > 10 \cdot n_k \cdot E_{br}$	Complete fragmentation

Figure 11.   Qualitative results for collisions between fractal dust aggregates [104]. The upper
left panel shows the initial condition with two equal-sized aggregates; the consecutive panels
show results of the collisions for increasing velocities.

the point of contact. The numerical agglomeration simulations presented in
section 3 represent that stage. At higher collision velocities, the monomer contact
can no longer hold the inertial forces of the impact, and some restructuring of the
aggregates occurs. This stage ends when the maximum mechanical compaction of
the aggregates is reached. At even higher impact velocities, the additional energy
is used for the break-up of monomer–monomer contacts within the aggregates.
At some stage, all contacts within the two colliding aggregates are broken,
and the aggregates are completely fragmented. Table 3 summarizes the results
and figure 11 shows examples of the numerical simulations by Dominik and
Tielens [104].

   A theoretical collision model, such as the one developed by Dominik and Tielens
[104], is only of limited practical use if its physical entities, i.e. the three parameters
n_k, E_{br} and E_{roll}, cannot be obtained empirically or experimentally. For fractal dust

aggregates with fractal dimensions $D_f \lesssim 2$, i.e. for those aggregates which preferentially form by CCA processes (see section 3), the number of contacts within an aggregate can be approximated by the number of monomer grains, $n_k = N$. This means that each monomer particle has on average two next neighbours, a value which can easily be comprehended by the CCA formation process. Thus, n_k can be obtained by the relation

$$n_k \approx \frac{m}{m_0}. \tag{109}$$

Here, m and m_0 are the mass of an aggregate and the mass of the constituent grain, respectively. For an independent determination of the break-up energy of a grain–grain contact, one can assume that this energy equals the energy in grain–grain collisions at the transition point between sticking and bouncing (see above). If the threshold velocity for sticking, v_s, is known, one gets

$$E_{br} = \frac{1}{4} m_0 v_s^2, \tag{110}$$

which is valid for collisions between two equal-mass dust grains†. Finally, the rolling-friction energy needs to be determined. Heim *et al.* [93, 106] showed how this can be done experimentally. In the earlier work, Heim *et al.* [93] formed aggregate chains consisting of a few dozen equal-sized spherical SiO$_2$ particles. Thereupon, they brought those particle chains between a piezo translation stage and the tip-less cantilever of an AFM. Applying an oscillatory motion to the piezo stage, Heim *et al.* [93] observed the reaction of the aggregate chain using a long-distance microscope and measured the applied force with the AFM. It turned out that the aggregates bent at one particle–particle contact, only, so that the AFM-measured force could be attributed to the rolling motion between this grain–grain contact (and additionally between the two contacts of those grains adjacent to the piezo stage and to the AFM cantilever). Recent experimental progress made it possible to observe the rolling of particle chains under the scanning electron microscope and simultaneously measure the contact forces [106] (figure 12). The derived rolling-friction forces between two SiO$_2$ spheres with radii of $s = 0.95\,\mu m$ are $F_{roll} = (8.5 \pm 1.6) \cdot 10^{-10}\,N$ [93]. Considering that there are two grains involved in rolling, one gets for the rolling-friction energy

$$E_{roll} = \pi s F_{roll} = O(10^{-15}\,J). \tag{111}$$

With the knowledge of the break-up and rolling-fiction energies, predictions for the outcomes of collisions of fractal dust aggregates can be made. These predictions can then be compared to the results of aggregate collisions observed in the laboratory. Blum and Wurm [107] performed impact experiments between fractal dust aggregates and dusty targets. They produced the dust aggregates in a rarefied turbulent gas and expanded the dust–gas mixture through a nozzle into vacuum.

---

†The pre-factor 1/4 results from the fact that the kinetic energy in a collision between two equal-mass grains with relative velocity v_s is $E_{kin} = \mu v_s^2/2$, where $m_0 \cdot m_0/(m_0 + m_0) = m_0/2$ denotes the reduced mass.
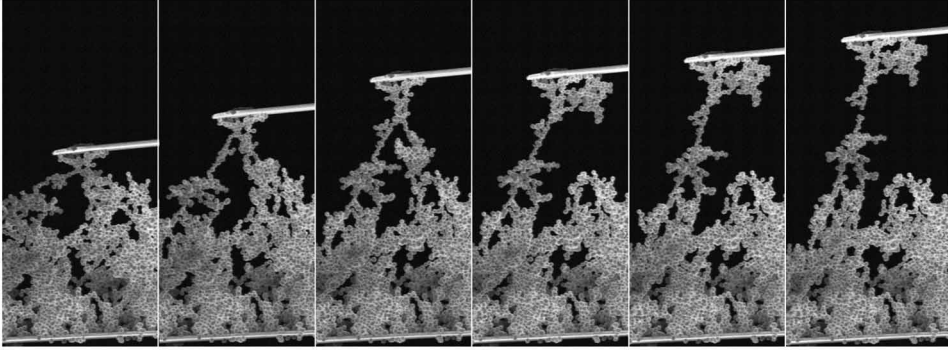
Figure 12. Determination of adhesion and rolling-friction forces in dust aggregates using atomic force microscopy [93, 106]. In the lower half of the images a dust aggregate is visible which is brought into contact with an AFM cantilever (near-horizontal bright object). Then, the AFM cantilever is moved upwards which causes the stretching and breaking of the particle chains. The bending of the AFM cantilever (measurable by the position of its front end with respect to the position of the [invisible] piezo translation stage) is a measure of the applied force. Particles in this example are SiO_2 spheres with $s = 0.75\,\mu m$.

Thus, a jet of fractal dust aggregates with fractal dimensions of $D_f = 1.91$ formed [9]. To prevent possible compaction due to gravitational aggregate restructuring (as observed in the laboratory, see [107]), the experiments were performed under microgravity conditions in a drop tower. For low impact velocity, Blum and Wurm [107] observed a perfect hit-and-stick behaviour of the aggregates, whereas for increasingly higher impact velocities, compaction and fragmentation were observed. This qualitative impact behaviour was observed for aggregates consisting of spherical SiO_2 particles with $0.5\,\mu m$ and $0.95\,\mu m$ radius as well as for aggregates consisting of irregular $MgSiO_3$ grains with sizes $< 1.25\,\mu m$. For a comparison to the aggregate collision model by Dominik and Tielens [104], Blum and Wurm [107] used the data on single-grain impacts by Poppe *et al.* [97] (equation 110) and on rolling-friction by Heim *et al.* [93] (equation 111) of SiO_2 spheres with $0.95\,\mu m$ radius. Using $n_k = m/m_0$ (see equation 109) and $E_{br} = 1.3 \cdot 10^{-15}\,J$ and $E_{roll} = 1.7 \cdot 10^{-15}\,J$, Blum and Wurm [107] get the results depicted in table 4. The correspondence between theoretical and experimental results is excellent so that the aggregate collision model by Dominik and Tielens [104] can be regarded as suitable for the collision behaviour of fractal dust aggregates.

The information one gets from the model by Dominik and Tielens [104] is that fractal dust aggregation cannot proceed infinitely long. When the impact energy exceeds $5 \cdot E_{roll}$, aggregates will change their fractal dimensions and become more compact as compared to their previous stage (see also section 3.1). It is worth mentioning that the threshold energy for restructuring is not proportional to the number of contacts in the aggregate. This is due to the fact that in a collision between fractal aggregates, the contact is always made between a single pair of monomers. Thus, the energy relevant for the decision whether restructuring occurs or not, is independent of the aggregate mass, whereas the collision energy is proportional to the aggregate mass. Thus, at a given impact velocity, larger aggregates restructure

Table 4. Comparison between experimental and theoretical results for the impact behaviour of fractal dust aggregates. The cases and energy ranges correspond to those shown in table 3. The experimental and theoretical threshold velocities were taken from [107] and [104], respectively. Experiments refer to fractal dust aggregates consisting of spherical SiO_2 particles with $0.95\,\mu m$ radius. The theoretical data were obtained using the model by Dominik and Tielens [104] with the values $n_k = 2$, $E_{br} = 1.3 \cdot 10^{-15}\,J$ and $E_{roll} = 1.7 \cdot 10^{-15}\,J$.

Case	Energy range	Experimental threshold velocity (m s^{-1})	Theoretical threshold velocity (m s^{-1})
(1)	$E_{im} < 5 \cdot E_{roll}$	< 0.20[a]	< 0.20[a]
(2)	$E_{im} \approx 5 \cdot E_{roll}$	0.20[a]	0.20[a]
(3)	$E_{im} \approx 1 \cdot n_k \cdot E_{roll}$	0.65	0.69
(4)	$E_{im} \approx 3 \cdot n_k \cdot E_{br}$	1.2	1.0
(5)	$E_{im} > 10 \cdot n_k \cdot E_{br}$	> 1.9	> 1.9

[a]This result is valid for $m = 60\,m_0$.

easier than small ones. This means that for any large-scale aggregation scenario one can expect that non-fractal aggregates form sooner or later. Thus, in the following section, the physics of non-fractal dust aggregates will also be considered.

It must be clarified that the Dominik and Tielens collision model for fractal aggregates is a coarse approximation to the impact behaviour of real fractal dust aggregates. For irregular, non-spherical grains, sliding friction [105] should also play some role in the restructuring process. Ecke and Butt [108] measured the friction force between micrometer-sized SiO_2 particles and flat SiO_2 substrates. They showed that the friction force is given by $F_f \propto \sigma_c$, where σ_c is the contact area between the particles. Typical values range between $F_f \approx 10^{-8}\,N$ and $F_f \approx 5 \cdot 10^{-7}\,N$, depending on the surface properties of the particles. Thus, these friction forces are much higher than the rolling-friction forces and are of the same order as the contact forces (see above).

5.4. Collisions between non-fractal dust aggregates

5.4.1. Formation of non-fractal aggregates in the laboratory.
In this section, it will be concentrated on non-fractal dust aggregates formed by a process analogous to the ballistic PCA process. The data in table 1 show that only the ballistic PCA aggregates are non-fractal. Due to the long formation times of macroscopic ballistic PCA particles, no experimental studies of these types of aggregates have been performed. However, there is a process which is nearly equivalent to ballistic PCA and leads to identical aggregate porosities. This process is named random ballistic deposition (RBD) and can be used to form macroscopic, non-fractal dust aggregates for empirical investigations. In its idealized form, RBD uses individual, spherical and monodisperse particles which are deposited randomly but unidirectionally on a semi-infinite target. A way to describe the morphology of the resulting RBD aggregates is by the volume filling factor ϕ, defined as the fraction of the volume filled by dust particles. The volume filling factor is related to the often-used porosity π by $\phi + \pi = 1$. Numerical simulations with up to 10^6 particles show that RBD agglomerates have $\phi = 0.1469 \pm 0.0004$ [109]. Thus, RBD agglomerates have much lower volume filling factors than the random close packing (RCP) which is the
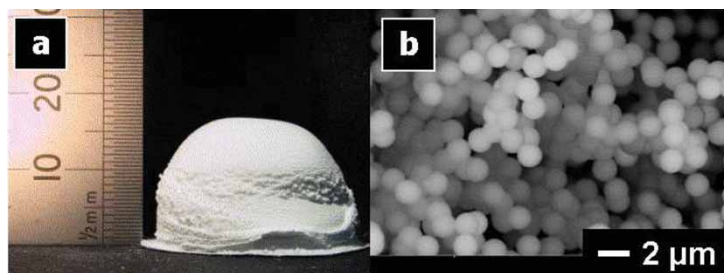
Figure 13.   Example of an aggregate grown by random ballistic deposition in the laboratory (a). The aggregate consists of SiO_2 spheres with $1.5\,\mu m$ diameter (b). The volume filling factor of this RBD aggregates is $\phi = 0.15$. Pictures are taken from [112]. Reproduced with permission [112]. © 2004, 1991 the American Physical Society.

densest configuration of randomly arranged monodisperse spherical particles. RCP has a volume filling factor of $\phi \approx 0.64$ (see e.g. [110]). The volume filling factor of ballistic PCA clusters is also $\phi = 0.15$ [62, 111]. In nature, the ballistic PCA process is expected when a bimodal size distribution of aggregates (in the idealized case: aggregates of one size and individual dust particles) is present and when the aggregation rates between the large aggregates and the small particles exceed those between all other combinations. Due to the similarity between RBD and ballistic PCA in the formation process and in the resulting aggregate structures and due to the fact that RBD agglomerates are easier to form in the laboratory, only the mechanical properties of the RBD aggregates have been investigated.

To simulate the 'ideal' RBD process in the laboratory, Blum and Schräpler [112] used monodisperse spherical SiO_2 particles with $0.75\,\mu m$ radius (figure 13). They deposited the single monomer grains on a filter substrate in a unidirectional rarefied-gas flow. The particle velocities at the deposition were so low that impact-induced grain restructuring (see section 5.3) was inhibited. Thus, the impinging particles stuck to the previously deposited particles in a hit-and-stick manner so that an RBD aggregate formed. One should mind, however, that the 'ideal' RBD aggregate is anisotropic. Due to its formation process, i.e. uniaxial impact of dust particles, an RBD aggregate consists of particle chains extending primarily in one spatial direction. In reality, those particle chains cannot grow infinitely long because gravity-induced rolling results in some restructuring [107]. Thus, due to gravity, the growing RBD aggregate gets slightly compacted and becomes more isotropic when the growing particle chains tilt. As the mean free path of the tilting particle chains is very short, the change in volume filling factor is unmeasurably small. Blum and Schräpler [112] experimentally find a volume filling factor of $\phi = 0.15$ for their samples of $2.5\,cm$ diameter, in good agreement with the RBD model.

5.4.2. Modelling of non-fractal aggregates.   The collision and aggregation properties of macroscopic dust aggregates can no longer be modelled by the interaction of all monomer grains in contact. Therefore, continuum properties are sought which characterize the collisions between high-porosity dust agglomerates. Sirono [113] developed a smooth particle hydrodynamics (SPH) code and found that the

collisions between dust aggregates can be treated in a continuum description when the compressive strength $\Sigma(\phi)$, the shear strength $Y(\phi)$, and the tensile strength $T(\phi)$ of the aggregates are known as functions of the aggregate density or volume filling factor ϕ. For sticking to occur in an aggregate–aggregate collision, Sirono found that the impact velocity must be smaller than 4% of the sound speed of the aggregate material. The sound speed can be calculated by

$$c(\phi) = \sqrt{\frac{\mathrm{d}\Sigma(\phi)}{\mathrm{d}\rho(\phi)}}, \tag{112}$$

where $\rho(\phi) = \rho_0 \cdot \phi$ is the mass density of the aggregate and ρ_0 denotes the mass density of the particle material. Moreover, the conditions $\Sigma(\phi) < Y(\phi)$ and $\Sigma(\phi) < T(\phi)$ must be fulfilled for sticking. For the shear strength, Sirono applied $Y(\phi) = \sqrt{2\Sigma(\phi)T(\phi)/3}$. A low compressive strength of the colliding aggregates favours compaction and, thus, damage restoration which can otherwise lead to a break-up of the aggregates. In addition, a large tensile strength also prevents the aggregates from being disrupted in the collision.

Sirono and Greenberg [114] and Greenberg *et al.* [115] derived expressions for the compressive and tensile strength of aggregated materials, based upon the interaction between individual dust particles. Following Sirono and Greenberg [114], the compressive strength is either dominated by rolling or by sliding friction. If one assumes that rolling friction is more important than sliding in aggregate restructuring [104, 105], the compressive strength is given by

$$\Sigma(\phi) = \frac{12\pi\gamma s\xi(N+1)}{l^2(N-3)}\left(\frac{l}{2}-s\right)^{-1}, \tag{113}$$

where γ, s and ξ are the specific surface energy of the particles (see equation 105), the particle radius and the length scale over which rolling is reversible and elastic [104, 105]. This length scale was empirically determined to be $\xi = 3.2$ nm for SiO_2 spheres with 0.95 µm radius [93]. Sirono and Greenberg [104, 105] assume periodically arranged 'cages' of particle chains consisting of N particles. The 'cages' have typical sizes of l. In this model, the volume filling factor can be expressed by

$$\phi = \frac{4\pi s^3(3N-5)}{3l^3}. \tag{114}$$

If one assumes $l \gg 2s$, one can substitute the unknown length scale of the 'cages' and get from equations (113) and (114)

$$\Sigma(\phi) = \frac{18\gamma\xi\phi}{s^2}\frac{(N+1)}{(N-3)(3N-5)} < \frac{13\gamma\xi\phi}{s^2} \tag{115}$$

for $N \geq 4$. For the SiO_2 dust samples produced by Blum and Schräpler [112] it was found that $\Sigma \leq 155$ Nm^{-2}, with $\gamma = 0.014$ Jm^{-2} [93], $\xi = 3.2$ nm [93], $\phi = 0.15$ [112] and $s = 0.75$ µm. However, for $l \to 2s$ the compressive strength can get very large. This should be the case for densely compressed dust agglomerates.

The tensile strength can be expressed by [115]

$$T(\phi) = \frac{3\nu_k \phi \gamma a_c^2}{4s^3}, \tag{116}$$

where ν_k and a_c are the average number of contacts per monomer grain inside the aggregate and the radius of the contact area between two spherical monomer grains. With the relation between the separation energy of a pair of monomer grains (see equation 110 and table 4) and the parameters γ and a_c,

$$E_{br} \approx 4.67\gamma \, a_c^2 \tag{117}$$

[104], one gets

$$T(\phi) \approx \frac{0.16\nu_k \phi E_{br}}{s^3}. \tag{118}$$

The number of contacts per monomer grain in any dust aggregate is close to $\nu_k = 2$. For $s = 0.75\,\mu$m SiO$_2$ spheres, extrapolations of the impact experiments by Poppe *et al.* [97] yields $E_{br} = 1.0 \cdot 10^{-15}$ J. Thus, one can expect with $\phi = 0.15$ a tensile strength of the aggregate of $T = 114$ Nm^{-2}.

The evaluation of equations 118 and 115 show $\Sigma \approx T$ so that the condition for sticking, $\Sigma(\phi) < Y(\phi)$ seems not to be fulfilled for high-porosity dust agglomerates. In the following, the theoretical estimations will be compared to empirical laboratory data which were published by Blum and Schräpler [112] and Blum *et al.* [116]. As mentioned above, Blum and Schräpler [112] developed an experimental setup for the formation of stable macroscopic dust agglomerates whose structures are analogous to RBD aggregates. Static uniaxial compression experiments with these samples showed that the volume filling factor is constant as long as the stress on the sample is below ~ 500 Nm^{-2}. For higher stresses, the volume filling factor slowly increases from $\phi = 0.15$ to $\phi = 0.33$. Above $\sim 10^5$ Nm^{-2}, the volume filling factor remains constant at $\phi = 0.33$. Thus, the compressive strength of the uncompressed sample is $\Sigma \approx 500$ Nm^{-2}. This is a factor of a few above the result of equation (115) derived for the same particle and aggregate parameters. Blum and Schräpler [112] also measured the tensile strength of their aggregates and found for slightly compressed samples ($\phi = 0.23$) $T = 1{,}100$ Nm^{-2}. After three-axial compression to $\phi = 0.41$ and $\phi = 0.66$, the tensile strength had increased to $T = 2{,}400$ Nm^{-2} and $T = 6{,}300$ Nm^{-2} [116]. A comparison to the theoretical value (equation 118) shows that the experimental results are about one order of magnitude higher. However, the tendency of the tensile strength to increase with increasing volume filling factor seems to be correct. One can explain the increase in tensile strength by a combination of an increased volume filling factor and the increase in the number of neighbours. Experiments with irregular particle shapes and/or a wide size range for the monomer grains showed very similar results [116]. Depending on the particle shape and the size distribution, the volume filling factor of the RBD aggregates decreased down to $\phi = 0.07$. The compressive strength and the tensile strength also decreased to values of $\Sigma \sim 200$ Nm^{-2} for the uncompressed case. Maximum compression of $\sim 10^6$ Nm^{-2} resulted in an increased volume filling factor that was as low as $\phi = 0.20$ for irregular grains with a wide size distribution [116]. Blum and

Schräpler [112] found an approximate relation between compressive strength and volume filling factor

$$\Sigma(\phi) = \Sigma_s(\phi - \phi_0)^{0.8},$$ (119)

which is valid in the range $\phi_0 = 0.15 \lesssim \phi \lesssim 0.21$. Such a scaling law was also found for other types of macroscopic aggregates, e.g. for jammed toner particles in fluidized bed experiments [117]. For the aggregates consisting of $1.5\,\mu m\,SiO_2$ spheres, the scaling factor is $\Sigma_s = 2.9 \times 10^4\,Nm^{-2}$. If one applies equation 119 to equation 112, One gets, with $\rho(\phi) = \rho_0 \cdot \phi$ and $\rho_0 = 2 \times 10^3\,kg\,m^{-3}$, for the sound speed of the low-density dust aggregates

$$c(\phi) = \sqrt{\frac{0.8\Sigma_s}{\rho_0(\phi - \phi_0)^{0.2}}} \approx 3.4\,(\phi - \phi_0)^{-0.1}\,ms^{-1}.$$ (120)

Although the function in equation 120 diverges for $\phi \to \phi_0$, for all practical purposes the sound speed is strongly restricted. For volume filling factors in the range $0.16 \leq \phi \leq 0.21$ one gets $5.4\,ms^{-1} \geq c(\phi) \geq 4.5\,ms^{-1}$. Thus, following the SPH simulations by Sirono [113], agglomerate sticking in collisions can be expected for impact velocities $v \lesssim 0.2\,ms^{-1}$. However, the validity of equation 112 for dust aggregates needs still to be proven.

5.4.3. Collisions between non-fractal aggregates. It was just shown that the experimental and theoretical results for the static compressive and tensile strengths differ by up to a factor 10. Let us now consider recent results in the field of high-porosity-aggregate collisions. Langkowski and Blum [118] performed collision experiments between $s \sim 0.1$–1 mm-sized (projectile) aggregates and 2.5 cm-sized (target) agglomerates. Both aggregates had volume filling factors of $\phi = 0.15$ and consisted of monodisperse spherical SiO_2 grains with radii of $s_0 = 0.75\,\mu m$. In addition to that, impact experiments with high-porosity aggregates consisting of irregular and/or polydisperse monomer grains were performed. As was shown above, the sticking threshold velocity for the individual monomer grains is $v_s \approx 1\,ms^{-1}$ (see equation 106). Thus, it is of special interest to investigate the collision behaviour of the dust aggregates in the velocity regime around $v = 1\,ms^{-1}$. The parameter space of the impact experiments by Langkowski and Blum [118] encompassed collision velocities in the range $0 < v < 3\,ms^{-1}$ and projectile masses of $10^{-9}\,kg \leq m \leq 5 \times 10^{-6}\,kg$ for all possible impact parameters (i.e. normal to tangential impacts). All experiments were performed under microgravity conditions so that no gravity-induced sticking could occur. One of the most interesting findings was that sticking between the projectile and the target dominated most of the parameter space (see left-hand side of figure 14 for an example). The experiments with aggregates consisting of monodisperse spherical SiO_2 grains showed a steep decrease in sticking probability (the parameter $\beta_a(j, i; v)$ in equation 67) with increasing impact parameter for mm-sized projectiles. This means that, while near-normal impacts lead to sticking, near-tangential collisions cause a rebound of the projectile. Smaller projectiles stuck at any impact angle. The other materials also show the tendency towards lower sticking probabilities with increasing
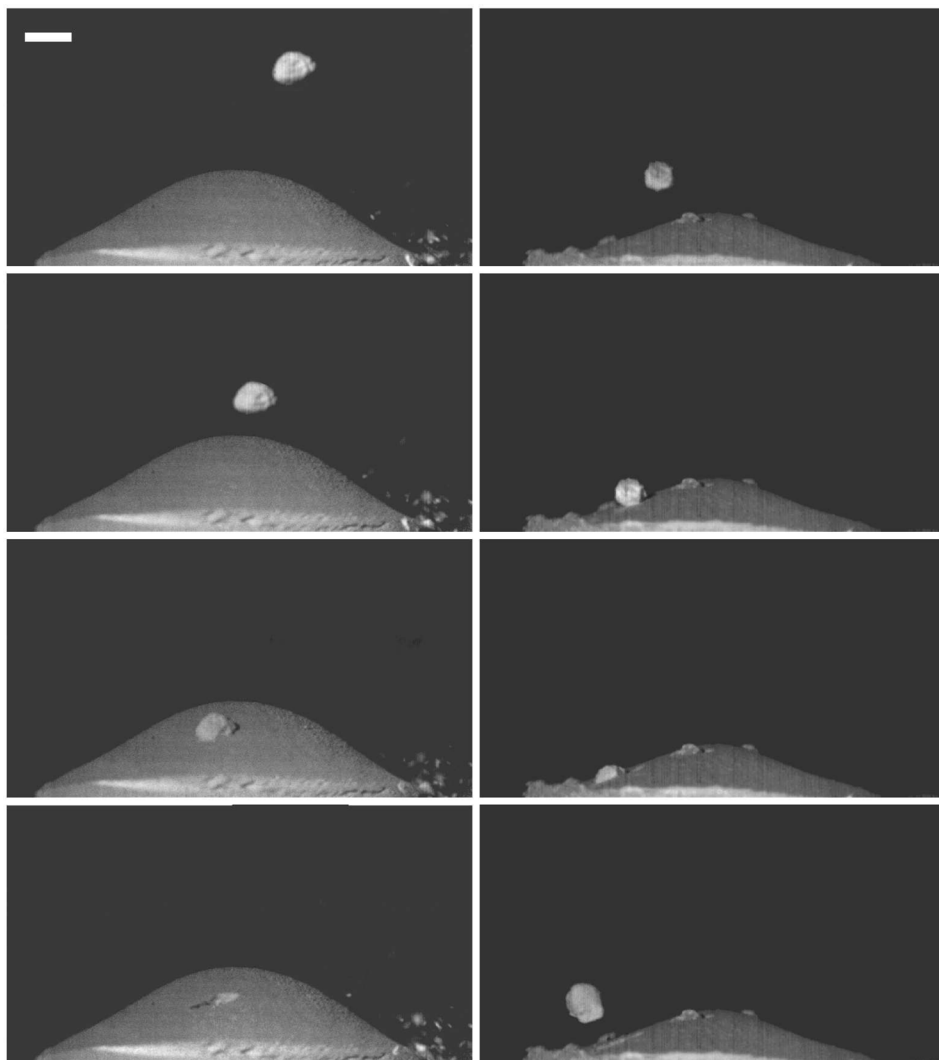
Figure 14. Examples of a sticking (left) and a non-sticking (right) collision between macroscopic dust aggregates grown by the RBD process at very similar impact conditions. The left column shows an impact of an agglomerate consisting of $1-2\,\mu m$ diamond particles into a target of the same composition. The impact velocity is $2.3\,ms^{-1}$ and the projectile and target volume filling factors are $\phi = 0.10$. Consecutive images were recorded each 2.2 ms. In the right column, an impact of an agglomerate consisting of spherical SiO_2 particles with $1.5\,\mu m$ diameter is shown. The impact velocity is $1.9\,m\,s^{-1}$ and the volume filling factors of projectile and target are $\phi = 0.15$. The first three images were recorded each 2.2 ms; the last image was taken 26.4 ms after the third image (from [118]). A mass transfer from the target to the projectile agglomerate is clearly visible. The scale bar in the upper left corner is 3 mm.

impact angle for the mm-sized projectiles. However, as these aggregates were 'softer' (i.e. have lower compressive strengths), the decline in sticking probability in the investigated parameter space is not complete. A steep transition between sticking and non-sticking was also present in the collision experiments between single projectile particles and smooth solid targets [97] (see section 5.2 and figure 10a) as well as between fractal dust aggregates [107] (see section 5.3). It is interesting to note that these different collision experiments show very similar threshold velocities of ~ 1 m s^{-1}, when the same constituent grains are used†.

In those cases in which the projectile agglomerates did not stick to the target agglomerate, it was found that a considerable mass transfer from the target to the projectile agglomerate had occurred during the impact (see right-hand side of figure 14). Typically, the mass of the projectile aggregate was doubled after a non-sticking collision. Formally, non-sticking collisions with mass transfer between projectile and target can be treated identical to the fragmentation case in Smoluchowski's equation (see equation 6 in section 2.1):

$$\left(\frac{\partial n(m, t)}{\partial t}\right)_{\mathrm{mt}} = \frac{1}{2}\int_0^\infty \int_0^\infty P_{\mathrm{mt}}(m; \bar{m}, m'; v) K_{\mathrm{mt}}(\bar{m}, m') n(\bar{m}, t) n(m', t) \mathrm{d}\bar{m} \mathrm{d}m'$$
$$- n(m, t)\int_0^\infty K_{\mathrm{mt}}(\bar{m}, m) n(\bar{m}, t)\mathrm{d}\bar{m}. \tag{121}$$

Here, $P_{\mathrm{mt}}(m; \bar{m}, m'; v)\mathrm{d}m$ is the probability that a collision between aggregates with masses m' and $\bar{m}$ results in a mass transfer such that one of the collision partners has a final mass in the range $m, \ldots, m + \mathrm{d}m$. $K_{\mathrm{mt}} = v(\bar{m}, m')\,\sigma(\bar{m}, m')$ is the ballistic collision kernel for non-fractal dust particles.

Langkowski and Blum [118] also determined some dynamical parameters which can help to characterize the physics of aggregate–aggregate collisions. The dynamically measured tensile strength was very similar to the static value. By estimating the crater volume V and assuming perfect plastic behaviour of the aggregates during impact‡ and the existence of a dynamic impact pressure p_{dyn} [119], one can state that the kinetic energy of the projectile E_{im} is completely absorbed by plastic flow so that one gets

$$p_{\mathrm{dyn}} = \frac{E_{\mathrm{im}}}{V} = \frac{mv^2}{2V}, \tag{122}$$

with m and v being the mass and velocity of the impinging projectile agglomerate. The experimental data from Langkowski and Blum [118] show that the dynamic pressure is indeed nearly constant and falls in the range $10^2, \ldots, 10^3$ Nm^{-2} for

---

†In all the presented cases in Refs. [97, 107, 118], one of the particle samples consisted of spherical SiO$_2$ grains with 1–2 μm diameter.
‡Perfect plasticity is not exactly fulfilled in the experiments as can be seen by a non-negligible rebound energy of the aggregates after a non-sticking collision (see right-hand side of figure 14).

projectile and target aggregates consisting of monodisperse spherical SiO_2 with $s = 0.75\,\mu m$ and $\phi = 0.15$. A comparison with the experiments by Blum and Schräpler [112] shows that their compressive strength for low filling factors is very similar to the dynamic pressure found in the impact experiments.

Blum and Münch [120] performed low-velocity collision experiments between pairs of $s = 1\,mm$ sized dust agglomerates. They used aggregates consisting of $s_0 = 0.2\ldots1\,\mu m$ $ZrSiO_4$ grains with a volume filling factor of $\phi = 0.26$. A comparison to the RBD aggregates produced by Blum and Schräpler [112] and Blum *et al.* [116] shows that the mm-sized aggregates of Blum and Münch were rather compacted. In their laboratory-scale microgravity experiment, Blum and Münch observed no sticking in the velocity range $v = 0.15,\ldots,3.9\,ms^{-1}$ for arbitrary impact parameters, in contrast to the findings by Langkowski and Blum [118]. The obvious differences between the two experiments are the volume filling factor and the larger radius of curvature of the samples used by Langkowski and Blum. Which of the two parameters determines the outcome of a collision needs to be investigated in future experiments. For collision velocities $v \gtrsim 2\,ms^{-1}$, Blum and Münch observed that the colliding projectiles preferentially fragmented and that the fragmentation mass loss is heavily dependent on the impact parameter in a way that it is largest for central collisions. The fragment mass distribution followed a power law

$$N_f(m')\,dm' = N_0 m'^\eta dm' \qquad (m' \in [m_0, m]), \qquad (123)$$

where $N_f(m')\,dm'$, N_0 and η denote the number of fragments in the mass range $m'\ldots m' + dm'$, a scaling factor and the exponent of the power law. Assuming collisions between equal-mass dust aggregates, mass conservation and an energy sink in fragmentation due to the formation of new agglomerate surface with a specific surface energy γ, Blum and Münch gave a relation† for the power-law exponent η from which one can derive

$$\frac{\eta + 2}{\eta + 5/3} \left[\frac{(m/m_0)^{\eta + 5/3} - 1}{(m/m_0)^{\eta + 2} - 1} \right] = \frac{1}{32\pi} \left(\frac{4\pi}{3} \right)^{2/3} \beta_e \phi^{2/3} \rho_0^{2/3} m_0^{1/3} \frac{v^2}{\gamma}, \qquad (124)$$

where β_e, ϕ, ρ_0, m_0 and m denote the efficiency with which kinetic energy is transferred into formation of new aggregate surface, the volume filling factor of the aggregates, the mass density of the monomer grains, the mass of the monomer grains and the masses of the colliding aggregates, respectively. Equations 123 and 124 enable one to use the extended Smoluchowski equation (through the parameter $P(m; \bar{m}, m'; v)$ in equation 7) also for the case of fragmentation.

It is interesting that by changing the experimental parameters to (1) different-sized projectiles, the larger one having $s = 1\,mm$, the smaller having an average mass ratio of 1/66 compared to the larger one, or (2) mm-sized projectiles made of low volume filling factor ($\phi = 0.03$) SiO_2 nanoparticles ($s_0 = 12 \pm 3$ nm),

†The constant c in [120] has a typing error and must be replaced by

$$c = \left[8\pi \left(\frac{3}{4\pi\rho} \right)^{2/3} \right]^{-1}.$$

collision experiments resulted in no sticking and no fragmentation [120]. In all collisions, a considerable kinetic energy loss was measured due to plastic flow of the aggregate material (dominating for central collisions) and due to transition from linear to rotational aggregate motion (dominating for grazing collisions).

In addition to the afore-described aggregate collisions at very low velocities, a few additional experimental investigations on the collision and sticking behaviour of loose dust aggregates have been performed. Wurm *et al.* [121] report on experiments in which several-millimeter-sized SiO_2 dust aggregates consisting of irregular, (sub)-micrometer-sized grains impact normally into 6 cm (diameter) dusty targets of the same material. The volume filling factors of the granular targets ranged between $\phi = 0.26$ and $\phi = 0.12$. Impact velocities were between $v = 16.5 \, \text{ms}^{-1}$ and $v = 37.5 \, \text{ms}^{-1}$. Wurm *et al.* observed the formation of impact craters whose volumes were several times larger than the volumes of the projectiles. However, many ejected fragments tended not to originate from the crater volume but were accelerated by elastic waves travelling along the surface of the target agglomerate. The total ejecta mass was up to ten times larger than the projectile mass. These fragments left the target with typical velocities of $\sim 0.005 \, v$.

Wurm *et al.* [122] studied central collisions between compacted dusty projectiles and targets. For volume filling factors of $\phi = 0.34$, very close to the maximum impact compaction derived by [103, 112, 116] (see above), they observed a transition between projectile rebound with limited fragmentation for $v \lesssim 13 \, \text{ms}^{-1}$ and sticking of large parts of the projectile for $v \gtrsim 13 \, \text{ms}^{-1}$. The mass transfer from the projectile to the target agglomerate was then typically 50% of the projectile mass. Wurm *et al.* [122] also observed the formation of small and fast ejecta at the highest impact velocities. Most of the ejecta were $< 500 \, \mu\text{m}$ in size and ejecta velocities could reach $\sim 0.4 \, v$. It is obvious that the compressibility of the colliding aggregates plays the decisive role for the outcome of a collision.

As was shown above, the compressive strength depends on the volume filling factor and particle size distribution [103, 112] for aggregates bound by van der Waals forces. However, thermal processing of dust aggregates can also lead to the solidification of the inter-particle bonds without changing the volume filling factor of the dusty object [123]. Even for temperatures considerably below the melting point, the formation of necks at the contact between two monomer grains by sintering is an important process with which the break-up energy for the inter-particle contacts can be increased by many orders of magnitude. Theoretical investigations as well as laboratory experiments (see, e.g., tables 3 and 4) have shown that the break-up energy is a crucial parameter for the determination of the outcome of a collision between two dust aggregates.

The theoretical and experimental investigations to describe the physics of aggregate collisions by means of a continuum theory have not yet resulted in a satisfying agreement. However, it was shown that macroscopic properties, such as the compressive and tensile strengths can be derived and measured for all kinds of non-fractal dust aggregates. These continuum quantities have the potential to be useful for the modelling of aggregate–aggregate collisions. For the realistic modelling of the evolution of aggregate sizes with time, it is important to describe the collision outcomes as perfectly as possible. Besides the afore-mentioned continuum

parameters, the formation of fragments plays a crucial role, particularly at higher impact velocities. Knowledge of fragment mass distributions (see equations 7, 123 and 124) and, for some simulations, also the distributions of fragment velocities and angles with respect to the target normal, is required for these kinds of simulations. Recent progress has been made in contact dynamics simulations of granular matter (see, e.g. [124]) in which the volume filling factors of macroscopic (non-fractal) dust aggregates can be derived as a function of cohesion and friction between the individual particles.

6. Observability of dust agglomeration

In this section, the techniques that are used for the analysis and characterization of dust aggregates in laboratory experiments will be reviewed. This will be particularly helpful for those readers who intend to start their own work on dust aggregation or particle analysis. The three most widely used techniques for particle characterization, i.e. sampling and counting (section 6.1), imaging (section 6.2) and light-scattering (section 6.3) will be presented. All three methods are capable of deriving information about the morphology and size distribution of dust agglomerates. These methods can be, and are, used in laboratory experiments on dust agglomeration as well as for the determination of the morphological properties of natural dust particles. One must distinguish between non-invasive investigations in which the system of dust aggregates remains unaltered by the observation and those methods that require particle sampling. Some of the methods described in the following subsections determine the aggregate morphology individually which means that a sufficiently large number of dust aggregates needs to be investigated to allow for the statistical description of the aggregation process. However, there are also some methods which determine some kind of average over a larger ensemble of dust aggregates. In that case, the averaging process, depending on the chosen method, needs to be known for a physical description of the aggregation scenario.

6.1. *Sampling and counting techniques*

Sampling is a widely used technique to identify and classify aerosol particles [1]. At ambient gas temperature and pressure, sampling can be accomplished in gas flows. By means of a test tube, a small part of the gas/dust mixture can be separated from the volume and then analyzed. However, for a quantitative determination of dust properties and number densities, it is essential to know whether the sampling method keeps the dust-to-gas ratio unchanged. It is therefore important that the sampling as such does not heavily interfere with the volume to be investigated. Friedlander [1] shows how the gas flow patterns change in the vicinity of the sampling probe if the ratio of the sampling velocity to gas velocity is varied. When sampling is done in a gas flow of known flow velocity, the *mass concentration* of the dust particles can be determined by *filtering* the solid constituents out of the gas. For the measurement of the *total number concentration* of particles a *condensation particle counter* or *condensation nuclei counter* can be used. This instrument uses the supersaturation of a vapor (e.g. water vapor) and its nature to preferentially condensate heterogeneously on pre-existing solid particles of any size. Thus, droplets

are formed from the supersaturated vapor with the same number density as that of the condensation nuclei present in the volume. The advantage is that the much larger droplets (typically in the size range of several micrometers) are easily detectable and countable by light-scattering methods (see section 6.3) whereas small, irregularly-shaped and possibly optically diverse solid particles are harder to quantify. *Particle sizes and size distributions* can be measured by (1) *light-scattering methods* (see section 6.3) and for single particles by a *single particle optical counter* which measures the absolute scattered light intensity which is – for known optical and morphological properties of the particles – a function of particle size. In addition to that, particle sizes can also be measured by (2) a *differential mobility analyzer* or *electrostatic classifier*, an instrument which uses a radioactive isotope for particle charging. The electrical mobility of the particles carrying a known number of elementary charges can then be measured in a strong electric field. The electrical mobility is a function of the grain size. The inertia of a dust particle and, hence, with some geometric assumptions, its size can also be estimated using (3) a *cascade impactor* which consists of a sequence of curved air-flow paths. Small particles are able to follow the air flow around obstacles which can be used as classifying samplers for the large particles that fall upon them. By varying geometry along the cascade, several size fractions are consecutively sorted out.

Under vacuum conditions or in rarefied gas environments, samples can be taken by moving or static collector plates at which the dust particles stick upon contact (see section 5.2 on sticking efficiencies). It must be noted that the capturing cross section of the collector plate depends on the Knudsen number, i.e. the ratio between the mean free path of the gas molecules and the size of the aggregates [125]. Inspection of these collector plates can be accomplished by optical or electron microscopy (see section 6.2).

6.2. *Imaging techniques*

The most straight-forward process to study the size and morphology of a dust aggregate relies on images from the particle. The optimal condition for the determination of the internal mass distribution of the aggregate is given when the optical resolution of the agglomerate image is much better than the size of the (smallest) monomer particle. Thus, optical microscopy is limited to constituent grain sizes of $\gtrsim 0.5\mu m$. When sampling of the dust aggregates is possible, electron microscopy can be used to determine exact grain positions within a dust aggregate. The spatial resolution of scanning electron microscopy (SEM) can be as high as a few nanometers. Even higher resolution can be gained by transmission electron microscopy (TEM) with which dust particles in the sub-nanometer size range can be resolved. Potentially, other scanning techniques with image capabilities, such as scanning tunnelling microscopy (STM) or atomic force microscopy (AFM) can also be used for the morphological characterization of dust aggregates. One should bear in mind that in general only two-dimensional information about the aggregate structure can be obtained by imaging techniques although stereo imaging was also used [79, 80]. The two-dimensional projection of an aggregate image bears two difficulties for the generation of three-dimensional structural information: (1) Only projected particle distances from the centre of the dust aggregate are available and

(2) dust grains in the 'foreground' of the image can (and will) obscure 'background' grains. However, Weitz and Oliveria [126] showed that for fractal dust aggregates with $D_f \leq 2$ the correct fractal dimension can be obtained even from the projected image [127].

If spatially resolved images of *many* dust aggregates are available, the fractal dimension of the aggregate ensemble can be determined following equation 71. For this, the aggregate mass and the radius of gyration (equation 72) must be measured.

A practical way to determine the fractal dimension of a *single* dust aggregate whose image or whose constituent-particle positions are available uses the space density–density correlation function [51]

$$C(\vec{r}) = \frac{\int_V \varphi(\vec{r'})\varphi(\vec{r}+\vec{r'})\mathrm{d}\vec{r'}}{\int_V \varphi(\vec{r'})\mathrm{d}\vec{r'}}, \tag{125}$$

where $\varphi(\vec{r})$ is the density of the aggregate at point $\vec{r}$ and V is the total volume of the particle. However, equation (125) is not straightforwardly useable. Typically, a digitized two-dimensional image of the dust aggregate is available on which either individual monomer grains or occupied/unoccupied sites are identifiable. If one binarizes the function $\varphi(\vec{r})$ such that it can obtain either $\varphi(\vec{r}) = 1$ for an occupied site or $\varphi(\vec{r}) = 0$ for an unoccupied site at position $\vec{r} = (x, y)$, the correlation function can be approximated by [51]

$$C(r) \approx \frac{1}{N}\sum_{r'} \varphi(r')\varphi(r+r'). \tag{126}$$

Here, $N = \sum_{r'} \varphi(r')$ is the total number of monomers/occupied sites within the dust aggregate and $r = \sqrt{x^2 + y^2}$ is the distance from the aggregate's center of mass. Plotting $C(r)$ as a function of r double-logarithmically will give a straight line with slope of $3 - D_f$ from which the fractal dimension of the aggregate can be computed.

Most microscopical imaging techniques require the sampling of dust aggregates prior to their structural investigation (see section 6.1). However, optical microscopy can also be used with rather long focal lengths so that non-invasive observations are possible. Krause and Blum [47] showed that even a direct mass determination of dust aggregates with low fractal dimensions is possible with a non-invasive long-distance microscopy technique. They used monodisperse spherical SiO_2 particles which have very small light absorption in the visible wavelength range. By using bright-field illumination in which the particles appear darker than the background, the light extinction (mainly due to diffraction and scattering) of each imaged dust aggregate can be measured. Division of the measured light extinction of the aggregates by the known value of the monomer grains allows the determination of the aggregate masses. Krause and Blum [47] calibrated the mass measurements in their method by the diffusion of the dust aggregates which they also observed. The diffusion constant of a single spherical dust particle is unambiguously determined by its size and, hence, its mass (equations 74–78).

6.3. *Light-scattering techniques*

If the spatial resolution of the system is not high enough or if the system cannot be observed with imaging techniques, the light scattered by individual dust aggregates or ensembles of dust particles can also be analysed to derive the sizes and size distributions of the aggregates. If the wavelength of the electromagnetic radiation used to measure the scattering efficiency is large compared to the aggregate size, i.e. $\lambda \gg s$, one can treat the dust aggregate as a Rayleigh particle. Hence, the intensity of the light scattered by one dust aggregate can be written as [1]

$$I(\theta) = I_0 \frac{8\pi^4}{\lambda^4 R^2} \alpha_p^2 (1 + \cos^2 \theta). \tag{127}$$

Here, I_0, R, α_p and θ are the unpolarized incident light intensity, the distance between the scattering particle and the observer, the polarizability of the dust aggregate and the scattering angle, respectively. The latter denotes the angle between the unscattered light beam and the direction in which the scattering is observed, i.e. $\theta = 0$ means forward and $\theta = \pi$ means backward scattering. As the polarizability of a spherical and isotropic particle is given by

$$\alpha_p = \frac{3(m^2 - 1)}{4\pi(m^2 + 2)} V, \tag{128}$$

proportional to the particle volume V and dependent on the complex refractive index m of the particle material, a single dust aggregate scatters light more effectively when its volume (and, thus, its mass) is larger. It is more practical to characterize the interaction of a dust particle with light by the particle's scattering and absorption efficiencies, Q_{sca} and Q_{abs}. These quantities are defined by the respective ratios of scattering and absorption cross section σ_{sca} and σ_{abs} to the geometrical cross section of the particle, i.e. $Q_{sca} = \sigma_{sca}/(\pi s^2)$ and $Q_{abs} = \sigma_{abs}/(\pi s^2)$. For Rayleigh particles, Q_{sca} and Q_{abs} can be written as [128]

$$Q_{sca} = \frac{8}{3} \chi^4 \mathrm{Re} \left(\frac{m^2 - 1}{m^2 + 2} \right)^2 \tag{129}$$

and

$$Q_{abs} = -4\chi \mathrm{Im} \left(\frac{m^2 - 1}{m^2 + 2} \right), \tag{130}$$

where $\chi = 2\pi s/\lambda$. It follows from equations (129) and (130) that for the scattering cross section $\sigma_{sca} \propto V^2$ and for the absorption cross section $\sigma_{abs} \propto V$. Thus, it can be distinguished between small and large dust aggregates by measuring the scattered light intensity. While the total absorbed light intensity will remain constant when the particles grow, due to the proportionality between Q_{abs} and V (as the number of absorbing particles decreases inversely with V), the total scattered light intensity, due to its proportionality to the square of the particle volume, will increase with increasing particle volume. Therefore, the mean aggregate size can in principle be

measured in an ensemble of dust particles by light scattering and absorption methods if the initial number density, the refractive index and the measurement volume are known.

If the dust aggregates are no longer small compared to the wavelength of the light, the light scattered from each atom in the dust particle interferes with that from all the other atoms. Thus, one gets a complex scattering function that depends on the aggregate size, its morphology and the scattering angle. Only for spherical particles [128] and a few other simple particle geometries (e.g. spherical particles having onion-shell structures, ellipsoids, infinitely long rods) does a closed solution to the scattering problem exist. In contrast to the Rayleigh limit where the light intensity scattered in a given direction can be used for the size determination of a dust aggregate, larger dust particles can more easily be characterized by their angular distribution of the elastically scattered light, $F(q)$. Here, q is the change in (the direction of) the wave vector from the incident light to the scattered light, and is related to the scattering angle by [129, 130]

$$q = \frac{4\pi}{\lambda} \sin\left(\frac{\theta}{2}\right). \tag{131}$$

For spherical particles of radius s, the scattering function is given by (see, e.g. [125])

$$F(x) = \left[\frac{3(\sin x - x \sin x)}{x^3}\right]^2, \tag{132}$$

with $x = qs$. For other particle geometries, the scattering function has also been derived. A compilation of scattering functions can be found in Takeo [125]. For fractal dust aggregates, Teixeira [131] describes how the scattering function can be obtained. It is interesting to note that for very large particles, i.e. for $s \gg \lambda$, the extinction efficiency is constant, $Q_{ext} = Q_{sca} + Q_{abs} = 2$, and both parts contribute equally, i.e. $Q_{sca} = Q_{abs} = 1$ in the geometric limit. However, this unusual behaviour can only be observed in the far field and for very small scattering angles. Experimental applications of the characterization of dust aggregates by the angular dependence of the light scattering intensity are widespread, both in the laboratory (see, e.g. [132]) and in nature, e.g. for the determination of the dust sizes in comets [133].

There are many more experimental methods for the determination of the aggregate structure and its fractal dimension available. As these are beyond the scope of this article, they shall only be briefly mentioned. For aggregates consisting of very small grains, small-angle X-ray scattering and small-angle neutron scattering were successfully applied. For very monochromatic light, Doppler shifts due to the Brownian motion of the particles can be used to obtain their masses. These methods are termed quasi-elastic light scattering, dynamic light scattering, or photon correlation spectroscopy. Inelastic light scattering methods use the Raman effect for the identification of chemical species in the dust particles. The scattering intensity with Raman scattering is proportional to the particle volume for $\chi > 0.2$ [1]. More information on these methods can be found in [1, 125].

7. An astrophysical application and open questions

Due to the author's background in astrophysics, the focus will be in applying the theoretical and experimental findings outlined in the preceding sections to models of the formation of dust aggregates in space. Smirnov [15] reviews several more applications of dust aggregation, such as the 'nuclear winter scenario', smoke particles from combustion processes, interplanetary dust particles collected in the stratosphere, mesospheric smoke stemming from meteor ablation, ceramics, and aqueous colloids. The interested reader is referred to the review by Smirnov and references therein. As already seen in section 1, Friedlander reviews the knowledge about aerosol physics [1].

For dust aggregation to occur in an astrophysical environment, the relative velocities between the dust grains must not be too high. In perfect vacuum or extremely rarefied gases, the orbital velocities of bodies about their central objects (stars, planets) are determined by Kepler's law and are typically a few to several hundred $km\,s^{-1}$. Thus, the *relative* velocity between two objects are determined by the orbital eccentricities and are therefore in such environments often not much below the orbital velocities and, thus, much too high for grain–grain sticking to occur†. Thus, the only environments in space in which considerable dust agglomeration can take place are those in which the gas densities are so high that the dust particles are more or less perfectly coupled to the gas flow. In such a scenario, the relative velocities between the dust grains can become very small. The objects with the highest gas densities in which dust particles can exist are molecular clouds, the accretion discs around forming stars (protoplanetary discs), the outer envelopes of cool giant stars and gaseous outflows of late-type or exploding stars (e.g. supernovae). In the following, it will be concentrated on dust-aggregation studies in protoplanetary discs, as this kind of aggregation spans the largest range in mass. Due to the relative unimportance of gravity for the dust-growth process in such systems, dust agglomeration is believed to be responsible for the growth in the size range from $\sim 1\,\mu m$ to $\sim 1\,km$ (see, e.g. [135]). Thus, dust agglomeration spans a mass range of ~ 27 orders of magnitude!

Stars form by the gravitational contraction of dense molecular clouds. Conservation of angular momentum in rotating systems‡ causes an asymmetry in the infall of matter towards the centre of gravity which results in the formation of a flattened disc due to the occurrence of centrifugal forces. Along the rotational axis of the disc, matter can freely fall onto the forming star, whereas perpendicular to this direction, matter can only be transported radially inward by the action of friction forces, i.e. in a viscous medium. Molecular viscosity is much too small to account for the observed rate of mass accretion. Other sources for viscosities, such as gas

---

†Exceptions are nanometer-sized dust grains for which sticking at $\sim km\,s^{-1}$ collision velocity might still be possible [2] and planetary ring particles whose individual orbits only marginally deviate from a perfect circle so that their relative velocities are very small [134].
‡Due to the differential rotation of the Galaxy, any extended part of it will have a non-zero angular momentum.

turbulence [136] and magneto-rotational turbulence [137] have been proposed. Protoplanetary discs are frequently observed in the wider galactic neighbourhood [138]. More and more investigations confirm that considerable growth of dust particles (by dust aggregation) happens in these environments [139–142].

The idea of dust aggregation in protoplanetary discs was pioneered by Weidenschilling [135, 143–147] who developed the first physical model of the processes which lead to gentle collisions between the dust grains and, in turn, to the formation of macroscopic dust aggregates. Weidenschilling [135, 143–147] identified as the major sources for dust–dust collisions Brownian motion, relative drift between two dust aggregates with different stopping times τ_f (see equations 85, 101–103), and gas turbulence, respectively. The analysis of the relative velocity pattern between the dust particles in such a disc showed that Brownian motion is important for small dust aggregates in the size range $s \sim 1, \ldots, 100\,\mu m$ (with decreasing collision velocities $v \lesssim 10^{-3}\,\mathrm{ms}^{-1}$ for increasing aggregate sizes), whereas the systematic drift motion and the influence of gas turbulence dominate the inter-particle collisions for larger aggregates. In the latter regime, a systematic increase of the collision velocity with increasing aggregate mass is expected for aggregates in the size range $s \sim 100\,\mu m \ldots 1\,m$. Between $s \sim 1\,m$ and $s \sim 1\,km$, the collision velocities do not change very much and are of the order of $v \sim 50\,\mathrm{ms}^{-1}$. For $s \gtrsim 1\,km$, gravitational effects dominate the interactions between dust aggregates so that the physics of dust aggregation as developed in the previous sections is no longer fully applicable. The typical size of a monomer dust grain from which dust aggregates are formed in protostellar accretion discs is assumed to be of the order of 1 micrometer.

With plausible assumptions about the development of the fractal dimension of the dust aggregates formed in sticking collisions, i.e. $D_f = 2.1$ for $s \leq 10^{-4}\,m$, $D_f = 2.1 \to 3$ for $10^{-4}\,m \leq s \leq 10^{-2}\,m$, $D_f = 3$ for $s \geq 10^{-2}\,m$, and a fragmentation model for high-velocity aggregate–aggregate collisions, Weidenschilling [135, 143–147] calculated the growth time scales and the growth mode of protoplanetary dust. He found that preferentially collisions between similar-sized macroscopic dust aggregates lead to the most efficient growth among the dust aggregates. The problem with this scenario is that there is no empirical information available about the outcome of aggregate–aggregate collisions for $\gtrsim 1\,m$-size (high-porosity) dusty objects and collision velocities $\gtrsim 1\,\mathrm{ms}^{-1}$. A consequence of Weidenschilling's model is that the forming km-sized bodies are porous, both on the microscopic and on the macroscopic level. If, on the other hand, the required stickiness of equal-sized dust aggregates is not physically feasible, the growth of the largest bodies might be dominated by particle–cluster aggregation (see section 3.1). As a consequence, the growing bodies would only exhibit considerable porosity on the microscopic level. Collisions among equal-sized bodies would result in a compaction and densification of the macroscopic dust aggregates (see sections 5.3 and 5.4) and possibly in fragmentation (see section 5.4). The resulting volume filling factors would then fall into the range $\phi = 0.20, \ldots, 0.33$ [103, 112]. Even if the sticking probability in collisions between small dust particles and macroscopic dust aggregates in the impact velocity range $v \gg 1\,\mathrm{ms}^{-1}$ is very low, a PCA-type growth could be present in young planetary systems. Wurm et al. [148, 149] pointed out that, due to the hydrodynamic circumstances, a 'headwind' exists that can drive

bouncing projectiles and/or emerging fragments back to the target body. An interesting discussion on the efficiency of this process can presently be followed in the literature [150–152]. Alternatively, Blum [103] pointed out that also electrical effects due to impact charging could result in an inevitable adhesion of small projectiles on macroscopic dusty targets.

Comets as the possible sole intact survivors of the formation phase of the solar system† play an important role in the testing of the above-described dust-aggregate formation models. Blum *et al.* [116] compiled results of measured cometary densities (and, with some plausible assumptions about the bulk density of cometary matter, of cometary volume filling factors ϕ) and found good agreement to laboratory results with RBD agglomerates‡ (see section 5.4.1). In addition to that, they also found that the tensile strengths of their laboratory RBD samples match those found in cometary meteoroids [155]. Unfortunately, the data on cometary densities cannot yet distinguish between porosity caused by macroscopic or microscopic voids. The European Space Agency's Rosetta project [156] will possibly shed some new light on the validity of the different formation scenarios.

Weidenschilling's model of the origin of km-sized bodies in the young solar system predicts formation timescales of $\sim 10^3, \ldots, 10^5$ years, depending on the radial distance from the sun. Based on the current empirical knowledge about aggregate–aggregate collisions, Blum [103] showed that decimeter-sized, non-fractal objects can form within ~ 500 years in the inner solar system. Further out, the timescales are much longer ($\sim 10^5$ years) and the maximum aggregate size for which reliable predictions can be made are much smaller (~ 1 mm).

While Weidenschilling's model considered the vertical transport of dust in circumstellar accretion discs during aggregation, more recent dust aggregation models in protoplanetary discs also take into account a more complex coupling between the dust and the accretion disc as a whole. Schmitt *et al.* [157] calculated the initial dust growth via Smoluchowski's equation for PCA and CCA aggregates and explicitly derived the dust opacity of the disc. The latter is an important quantity for the radiative energy transport in the protoplanetary disc and cannot be treated separately from the growth process. Radiation transport is essential for the analysis of images of protoplanetary discs which can only be interpreted with proper modelling. In addition to that, observations of spectral energy distributions of star-forming regions can also only be interpreted when the energy transfer from deep within the protoplanetary accretions discs to the observable surface (where the optical depth is $\lesssim 1$) is well understood. It is obvious that the spectral energy distribution of such

---

†If that assumption is true, comets are the largest dust aggregates known. That comets indeed contain vast amounts of dust particles can be seen by the huge cometary comae and dust tails that form when comets approach the sun. In addition to that, the recent Deep Impact mission impressively confirmed the dusty nature of comets when it launched a 362 kg projectile into the nucleus of comet 9P/Tempel 1 and released several thousand tonnes of dust [153].
‡The perhaps most accurate estimate of a cometary bulk density to date was obtained recently for Comet 9P/Tempel 1, as a result of the NASA *Deep Impact* mission, $\rho_{\text{bulk}} = 400 \pm 300 \, \text{kg m}^{-3}$ [154] which shows clear evidence of a very porous body.

objects not only depends on the spatial distribution of the dust but also on the size and morphology of the dust aggregates.

Dullemond and Dominik [158] developed an elaborate two-dimensional dust growth model for protoplanetary discs. They included coagulation via Smoluchowski's equation and fragmentation of dust aggregates which were assumed to be either spherical, of PCA, or of CCA type. In some of their models, aggregate fragmentation was assumed to occur when the specific collision energies were $E/m > 0.125\,\mathrm{J\,kg}^{-1}$ and was modelled to result in the complete conversion of the aggregate into its constituent monomer grains. Relative velocities between the grains were due to Brownian motion, differential settling and gas turbulence. The dust opacities and resulting spectral energy distributions were calculated and compared to modern observations of protoplanetary discs. Except for the initial stages, in which Brownian motion dominates, and those cases in which small particles are replenished by fragmentation, the model predicts a much lower abundance of small dust aggregates than derived by observations. The authors conclude that there must be either an external source of small dust particles or fragmentation is indeed an important process in protoplanetary accretion discs.

As just mentioned, a comparison between observations and models and, thus, an analysis of the physics of dust aggregation in protoplanetary discs, relies on an exact treatment of the radiative energy transfer within the discs. Therefore, an efficient 3D radiative transfer code [159–161] must be available and the optical properties of dust aggregates must be known (see also section 6.3). Of particular importance are dust aggregates whose sizes are comparable to the wavelength of the radiation used for the astronomical observations. For these sizes, the aggregate morphology plays an important role for their interaction with light. Many light-scattering models for dust aggregates and astrophysical applications were published [62, 162–165], but a 'simple' treatment of the aggregate-light interaction seems not possible.

Although considerable progress has been made in the past years in the laboratory as well as in modelling dust agglomeration in protoplanetary discs, there are several open questions still to be addressed. These outstanding questions comprise a physical model that describes the low-velocity collisional interaction of macroscopic dust aggregates, including the effects of particle adhesion, compaction and fragmentation. The SPH approach mentioned in section 5.4.2 seems to be best suited for this purpose. However, a thorough calibration of the existing codes with benchmark laboratory experiments has not been made. With such a code available, a thorough mapping of preplanetesimal aggregate collisions could be performed whose results could then be introduced into a kinetic description of aggregation by Smoluchowski's equation. Then, the growth of dust particles to km-sized bodies can be realistically modelled. An important observational aspect of this approach is that such a model would predict the size distribution of dust aggregates for all distances from the central star and for all evolutionary phases of the protoplanetary disc. Due to the decreasing surface-to-mass ratio of growing non-fractal dust agglomerates, they are generally unobservable once they have reached cm sizes. Thus, the direct detection of macroscopic dust aggregates in planet-forming regions is impossible.

Very large bodies, whose gravitational interaction with the gas-dust disc is no longer negligible, open gaps or excite spiral waves (see e.g. [166]) in their embedding discs which are observable phenomena. However, dust aggregates in the range between ∼1 cm and ∼1 km are too small to have a considerable gravitational influence on the disc. Thus, the only way of 'proving' the existence of dust aggregates in this size range is by their mutual collisional interaction. Here, the collisional fragmentation is the dominating process. While there is still no collision and fragmentation model available for dust aggregates, a comprehensive experimental and numerical study of aggregate–aggregate fragmentation could be the clue for a future interpretation of astronomical observations of protoplanetary discs.

Recently, the role of photophoresis in planet formation has been discussed [167, 168]. Photophoresis [169] is based upon the simultaneous interaction of a dust particle with electromagnetic radiation and with the ambient gas. Due to (partial) absorption of starlight, the dust aggregates experience a temperature gradient along their surfaces. Thus, collisions of gas molecules with a differentially heated surface lead to a net momentum transfer between dust and gas so that a relative motion between the dust aggregates and the gas occurs. In the free-molecular flow regime, the photophoretic velocity of the dust particles increases with increasing particle size and with decreasing thermal conductivity of the dust-aggregate material [169]. As high-porosity dust aggregates have very low thermal conductivities, their photophoretic velocity can be non-negligible [167]. Steinbach *et al*. [170] have experimentally shown that larger dust aggregates do indeed possess higher photophoretic velocities than smaller particles. Krauß and Wurm [167] and Wurm and Krauß [168] propose that photophoresis could be responsible for some observed ring structures in circumstellar discs and in debris discs and for the transport and size sorting of chondrules†. As chondrules have formed in the earliest stages of the planet formation in the solar system, knowledge about their formation, transport and embedding into their asteroidal parent bodies might reveal insight into the evolution of the first macroscopic solid bodies in the solar system.

---

†Chondrules are mm-sized melt droplets frequently found in primitive meteorites.

References

[1] S.K. Friedlander, *Smoke, Dust and Haze* (Wiley–Interscience, New York, 1972 and 2000).
[2] P. Reissaus, T. Waldemarsson, J. Blum, D. Clément, I. Llamas, H. Mutschke and F. Giovane, J. Nanoparticle Res., **8** 693 (2006).
[3] M.v. Smoluchowski, Physik. Zeit. **17** 557 (1916).
[4] R.M. Ziff, E.D. Mcgrady and P. Meakin, J. Chem. Phys. **82** 5269 (1985).
[5] G.W. Mulholland and R.D. Mountain, J. Chem. Phys. **84** 4109 (1986).
[6] D. Fry, T. Sintes, A. Chakrabarti and C.M. Sorensen, Phys. Rev. Lett. **89** 148301 (2002).
[7] G. Nicolis and E. Prigogine, *Exploring Complexity — An Introduction* (W.H. Freeman, New York, 1989).
[8] V. Ossenkopf, Astron. Astrophys. **280** 617 (1993).
[9] G. Wurm and J. Blum, Icarus **132** 125 (1998).
[10] R.M. Ziff, in: *Kinetics of Aggregation and Gelation*, edited by F. Family and D.P. Landau (Elsevier Science Publishers, North-Holland, 1984), pp. 191–199.
[11] M.H. Ernst, in: *Fractals in Physics*, edited by L. Pietronero and E. Tosatti (Elsevier Science Publishers, North-Holland, 1985), pp. 289–302.
[12] P.G.J. van Dongen and M.H. Ernst, Phys. Rev. Lett. **54** 1396 (1985).
[13] F. Leyvraz, in: *On Growth and Form*, edited by H.E. Stanley and N. Ostrowsky (Martinus Nijhoff Publishers, Dordrecht, 1986), pp. 136–144.
[14] R. Julliet and R. Botet, *Aggregation and Fractal Aggregates* (World Scientific, Singapore, 1987).
[15] B.M. Smirnov, Physics Reports **188** 1 (1990).
[16] M.v. Smoluchowski, Zeit. Phys. Chem. **92** 129 (1917).
[17] R.L. Drake, in: *Topics in Current Aerosol Research*, Vol. 3, edited by G.M. Hidy and J.R. Brock (Pergamon Press, New York, 1972), pp. 201–376.
[18] A.M. Golovin, Bull. Acad. Sci. USSR, Geophys. Ser. **5** 482 (1963).
[19] R.M. Ziff, M.H. Ernst and E.M. Hendriks, J. Phys. A: Math. Gen. **16** 2293 (1983).
[20] L. Binglin, J. Phys. A: Math. Gen. **20** 2347 (1987).
[21] R.P. Treat, J. Phys. A: Math. Gen. **23** 2003 (1990).
[22] R.L. Drake and T.J. Wright, J. Atmos. Sci. **29** 548 (1972).
[23] M.H. Lee, Icarus **143** 74 (2000).
[24] T. Vicsek and F. Family, *Fractal Growth Phenomena* (World Scientific, Singapore, 1984).
[25] D.S. Krivitsky, J. Phys. A: Math. Gen **28** 2025 (1995).
[26] N. Fournier and P. Laurençot, Commun. Math. Phys. **256** 589 (2005).
[27] M.H. Lee, J. Phys. A: Math. Gen. **34** 10219 (2001).
[28] M. Escobedo, S. Mischler and M. Rodriguez Ricard, Ann. I. H. Poincaré **AN 22** 99 (2005).
[29] P.B. Dubovskii, V.A. Galkin and I.W. Stewart, J. Phys. A: Math. Gen. **25** 4737 (1992).
[30] S. Simons, J. Phys. A: Math. Gen. **29** 1139 (1996).
[31] J.E.L. Bishop and T.M. Searle, Mon. Not. Roy. Astron. Soc. **203** 987 (1983).
[32] K. Ohtsuki, Y. Nakagawa and K. Nakazawa, Icarus **83** 205 (1990).
[33] S. Inaba, H. Tanaka, K. Ohtsuki and K. Nakazawa, Earth, Planets, and Space **51** 205 (1990).
[34] L. Malyshkin and J. Goodman, Icarus **150** 314 (2001).
[35] P. Goldreich, Y. Lithwick and R. Sari, Ann. Rev. Astron. Astrophys. **42** 549 (2004).
[36] G.A. Niklasson, A. Torebring, C. Larsson, C.G. Grangvist and T. Farestam, Phys. Rev. Lett. **60** 1735 (1988).
[37] G. Helgesen, A. Skjeltorp, P.M. Mors, R. Botet and R. Jullien, Phys. Rev. Lett. **61** 1736 (1988).
[38] A.B. Eriksson and M. Jonson, Phys. Rev. B **40** 884 (1989).
[39] C.F. Mors, R. Botet and R. Jullien, J. Phys. A **20** L975 (1987).
[40] P. Meakin, J. Colloid Interface Sci. **134** 235 (1990).
[41] G. Wurm and J. Blum, Astrophys. J. **529** L57 (2000).
[42] J.A. Nuth, J. Faris, P. Wasilewski and O. Berg, Icarus **107** 155 (1994).

[43] J.A. Nuth and G.M. Wilkinson, Icarus **117** 431 (1995).
[44] H. Nübold and K.-H. Glassmeier, Icarus **144** 149 (2000).
[45] C. Dominik and H. Nübold, Icarus **157** 173 (2002).
[46] H. Nübold, T. Poppe, M. Rost, C. Dominik and K.-H. Glassmeier, Icarus **165** 195 (2003).
[47] M. Krause and J. Blum, Phys. Rev. Lett. **93** 021103 (2004).
[48] A.V. Ivlev, G.E. Morfill and U. Konopka, Phys. Rev. Lett. **89** 195502 (2002).
[49] J.R. Marshall, T.B. Sauke and J.N. Cuzzi, Geophys. Res. Lett. **32** L11202 (2005).
[50] A. Einstein, Ann. Phys. **17** 549 (1905).
[51] T.A. Witten and L.M. Sander, Phys. Rev. Lett. **47** 1400 (1981).
[52] M.J. Vold, J. Colloid Interf. Sci. **14** 168 (1959).
[53] M.J. Vold, J. Colloid Interf. Sci. **18** 684 (1963).
[54] D.N. Sutherland, J. Colloid Interf. Sci. **22** 300 (1966).
[55] T.A. Witten and L.M. Sander, Phys. Rev. B **27** 5686 (1983).
[56] P. Meakin, Phys. Rev. A **27** 604 (1983).
[57] P. Meakin, Phys. Rev. A **27** 1495 (1983).
[58] P. Meakin, Phys. Rev. Lett. **51** 1119 (1983).
[59] M. Kolb, R. Botet and R. Jullien, Phys. Rev. Lett. **51** 1123 (1983).
[60] P. Meakin, Ann. Rev. Phys. Chem. **39** 237 (1988).
[61] M. Kostoglou and A.G. Konstandopoulos, Aerosol Science **32** 1399 (2001).
[62] T. Kozasa, J. Blum and T. Mukai, Astron. Astrophys. **263** 423 (1992).
[63] D. Paszun and C. Dominik, Icarus **182** 274 (2006).
[64] P. Meakin and R. Jullien, J. Chem. Phys. **89** 246 (1988).
[65] R. Jullien and P. Meakin, J. Colloid Interf. Sci. **127** 265 (1989).
[66] P. Meakin, Rev. of Geophys. **29** 317 (1991).
[67] D.K. Hutchins, M.H. Harper, and R.L. Felder, Aerosol. Sci. Technol. **22** 202 (1995).
[68] C.N. Davies, Proc. Phys. Soc. **57** 259 (1945).
[69] J.H. Kim, G.W. Mulholland, S.R. Kukuck and Y.H. Pui, J. Res. Natl. Inst. Stand. Technol. **110** 31 (2005).
[70] J. Blum, G. Wurm, S. Kempf and T. Henning, Icarus **124** 441 (1996).
[71] R. Nakamura and Y. Hidaka, Astron. Astrophys. **340** 329 (1998).
[72] P. Wiltzius, Phys. Rev. Lett. **58** 710 (1987).
[73] C.W. Ormel, M. Spaans and A.G.G.M. Tielens, Astrophys. J., in press.
[74] S. Kempf, S. Pfalzner and T. Henning, Icarus **141** 388 (1999).
[75] P. Epstein, Phys. Rev. **22** 710 (1923).
[76] J.-W. Kim and T.A. Kramer, Colloids and Surfaces A: Physicochem. Eng. Aspects **253** 33 (2005).
[77] J. Blum, M. Schnaiter, G. Wurm and M. Rott, Rev. Sci. Instrum. **67** 589 (1996).
[78] T. Poppe, J. Blum and T. Henning, Rev. Sci. Instrum. **68** 2529 (1997).
[79] J. Blum, G. Wurm, T. Poppe, T., *et al.*, Measurement Science & Technology **10** 836 (1999).
[80] J. Blum, G. Wurm, S. Kempf, *et al.*, Phys. Rev. Lett. **85** 2426 (2000).
[81] G.E. Uhlenbeck and L.S. Ornstein, Phys. Rev. **36** 823 (1930).
[82] E.J. Hinch, J. Fluid. Mech. **72** 499 (1975).
[83] B. Lukić, S. Jeney, C. Tischer, A.J. Kulik, L. Forró and E.-L. Florin, Phys. Rev. Lett. **95** 160601 (2005).
[84] S. Vemury and S.E. Pratsinis, J. Aerosol Sci. **21** 175 (1995).
[85] M. Zurita-Gotor and D.E. Rosner, J. Colloid Interf. Sci. **274** 502 (2004).
[86] S.K. Friedlander and G.M. Hidy, in: *Proceedings of the 7th International Conference on Condensation and Ice Nuclei*, edited by J. Podzimek (Academia, Prague, 1969).
[87] T. Matsoukas and S.K. Friedlander, J. Colloid Interf. Sci. **146** 495 (1991).
[88] P. Meakin, B. Donn and G. Mulholland, Langmuir **5** 510 (1989).
[89] H.C. Hamaker, Physica **4** 1058 (1937).
[90] H.-J. Butt, K. Graf and M. Kappl, *Physics and Chemistry of Interfaces* (Wiley–VCH, Weinheim, 2003).
[91] J.N. Israelachvili, *Intermolecular and Surface Forces* (Academic Press, San Diega, 1992).
[92] B.V. Derjaguin, V.M. Muller and Y.P. Toporov, J. Colloid Interf. Sci. **53** 314 (1975).

[93] L. Heim, J. Blum, M. Preuss and H.-J. Butt, Phys. Rev. Lett. **83** 3328 (1999).
[94] W.A. Ducker, T.J. Senden and R.M. Pashley, Nature **353** 239 (1991).
[95] H.-J. Butt, Biophys. J. **60** 1438 (1991).
[96] M. Morgeneyer, *Mechanische Eigenschaften kohäsiver Schüttgüter* (Clemens Eichorn Verlag für Hochschulschriften, Braunschweig, 2004).
[97] T. Poppe, J. Blum and T. Henning, Astrophys. J. **533** 454 (2000).
[98] A. Chokshi, A.G.G.M. Tielens and D. Hollenbach, Astrophys. J. **407** 806 (1993).
[99] B.E. Dahneke, J. Colloid Interf. Sci. **1** 58 (1975).
[100] F.G. Bridges, K.D. Supulver, D.N.C. Lin, *et al.*, Icarus **123** 422 (1996).
[101] T. Poppe, J. Blum and T. Henning, Astrophys. J. **533** 472 (2000).
[102] T. Poppe and R. Schräpler, Astron. & Astrophys. **438** 1 (2005).
[103] J. Blum, in: *Astrophysics of Dust*, edited by A. Witt, G. Clayton and B. Draine (ASP Conference Series, Vol. 309, 2004), pp. 369–391.
[104] C. Dominik and A.G.G.M. Tielens, Astrophys. J. **480** 647 (1997).
[105] C. Dominik and A.G.G.M. Tielens, Philosoph. Mag. A **72** 783 (1995).
[106] L. Heim, H.-J. Butt, R. Schräpler and J. Blum, Aus. J. Chem. **58** 671 (2005).
[107] J. Blum and G. Wurm, Icarus **143** 138 (2000).
[108] S. Ecke and H.-J. Butt, J. Colloid Interf. Sci.. **244** 432 (2001).
[109] P.K. Watson, H. Mizes, A. Castellanos and A. Pérez, in: *Powders & Grains 97*, edited by R. Behringer and J.T. Jenkins (Balkema, Rotterdam, 1997), pp. 109–112.
[110] S. Torquato, T.M. Truskett and P.G. Debenedetti, Phys. Rev. Lett. **84** 2064 (2000).
[111] P. Meakin, in: *On Growth and Form*, edited by H.E. Stanley and N. Ostrowsky (Martinus Nijhoff Publishers, Dordrecht, 1986), pp. 111–135.
[112] J. Blum and R. Schräpler, Phys. Rev. Lett. **93** 115503 (2004).
[113] S. Sirono, Icarus **167** 431 (2004).
[114] S. Sirono and J.M. Greenberg, Icarus **145** 230 (2000).
[115] J.M. Greenberg, H. Mizutani and T. Yamamoto, Astron. Astrophys. **295** L35 (1995).
[116] J. Blum, R. Schräpler, B.J.R. Davidsson and J.M. Trigo-Rodríguez, Astrophys. J. **652** 1768 (2006).
[117] J.M. Valverde, M.A.S. Quintanilla and A. Castellanos, Phys. Rev. Lett. **92** 258303 (2004).
[118] D. Langkowski and J. Blum, unpublished data.
[119] K.L. Johnson, *Contact Mechanics* (Cambridge University Press, Cambridge, 1985).
[120] J. Blum and M. Münch, Icarus **106** 151 (1993).
[121] G. Wurm, G. Paraskov and O. Krauss, Phys. Rev. E **71** 021304 (2005).
[122] G. Wurm, G. Paraskov and O. Krauss, Icarus **178** 253 (2005).
[123] T. Poppe, Icarus **164** 139 (2004).
[124] D. Kadau, G. Bartels, L. Brendel and D.E. Wolf, Phase Transitions: A Multinational Journal **76** 315 (2003).
[125] M. Takeo, *Disperse Systems* (Wiley–VCH, Weinheim, 1999).
[126] D.A. Weitz and M. Oliveria, Phys. Rev. Lett. **52** 1433 (1984).
[127] J.A. Nelson, R.J. Crookes and P. Simons, J. Appl. Phys. **23** 465 (1990).
[128] H.C. van de Hulst, in: *Light Scattering by Small Particles* (Wiley, New York, 1957).
[129] Lord Rayleigh, Proc. Roy. Soc. **A90** 219 (1914).
[130] P.N. Pusey, in: *Colloidal Dispersion*, edited by J. W Goodwin (Royal Society of Chedmistry, London, 1982).
[131] J. Teixera, in: *On Growth and Form*, edited by H.E. Stanley and N. Ostrowsky (Martinus Nijhoff Publishers, Dordrecht, 1986), pp. 145–162.
[132] E. Hadamcik, J.–B. Rénard, A.-C. Levasseur-Regoard and J.-C. Worms, Journal of Quantitative Spectroscopy & Radiative Transfer **79–80** 679 (2003).
[133] L. Kolokolova, M.S. Hanner, A.-C. Levasseur-Regourd, and B.Å.S. Gustafson, in: *Comets II*, edited by M.C. Festou, H.U. Keller and H.A. Weaver (University of Arizona Press, Tucson, 2004), pp. 577–604.
[134] P. Goldreich and S. Tremaine, Ann. Rev. Astron. Astrophys. **20** 249 (1982).
[135] S.J. Weidenschilling and J.N. Cuzzi, in: *Protostars and Planets III*, edited by E. Levy and J.I. Lunine (University of Arizona Press, Tucson, 1993), pp. 1031.

[136] H.J. Völk, G.E. Morfill, S. Roeser and F.C. Jones, Astron. Astrophys. **85** 316 (1980).

[137] S.A. Balbus and J.F. Hawley, Astrophy. J. **376** 214 (1991).

[138] M.J. McCaughrean and C.R. O'dell, Astronom. J. **111** 1977 (1996).

[139] R. van Boekel, M. Min, L.B.F.M. Waters, *et al.*, Astron. Astrophys. **437** 189 (2005).

[140] T. Henning, C.P. Dullemond and S. Wolf, in: *Planet Formation. Theory, Observation and Experiments*, edited by H. Klahr and W. Brandner (Cambridge University Press, Cambridge, 2006).

[141] L. Testi, A. Natta, D.S. Shepherd and D.J. Wilner, Astron. Astrophys. **403** 323 (2005).

[142] D.J. Wilner, P. D'Alessio, N. Calvet, M.J. Claussen and L. Hartmann, Astrophys. J. **626** L109 (2005).

[143] S.J. Weidenschilling, Icarus **44** 172 (1980).

[144] S.J. Weidenschilling, Icarus **60** 553 (1984).

[145] S.J. Weidenschilling, Gerlands Beiträge zur Geophysik **96** 21 (1987).

[146] S.J. Weidenschilling and T.V. Ruzmaikina, Astrophys. J. **430** 713 (1994).

[147] S.J. Weidenschilling, Icarus **127** 290 (1997).

[148] G. Wurm, J. Blum and J.E. Colwell, Phys. Rev. E **64** 046301 (2001).

[149] G. Wurm, J. Blum and J.E. Colwell, Icarus **151** 318 (2001).

[150] M. Sekyia and H. Takeda, Earth, Planets and Space **55** 263 (2003).

[151] G. Wurm, G. Paraskov and O. Krauss, Astrophys. J. **606** 983 (2004).

[152] M. Sekyia and H. Takeda, Icarus **176** 220 (2005).

[153] M. Küppers, I. Bertini, S. Fornasier, *et al.*, Nature **437** 987 (2005).

[154] J.E. Richardson and H.J. Melosh, Lunar Planet. Sci. **XXXVII** 1836 (2006).

[155] J.M. Trigo-Rodríguez and J. Llorca, Mon. Not. Roy. Astron. Soc. **372** 655 (2006).

[156] C. Berner, L. Bourillet, J. van Casteren, J. Ellwood, M. Kasper, P. Kletzkine, R. Schulz, G. Schwehm, M. Warhaut and P. Bond, ESA Bulletin **112** 10 (2002).

[157] W. Schmitt, T. Henning and R. Mucha, Astron. Astrophys. **325** 569 (1997).

[158] C.P. Dullemond and C. Dominik, Astron. Astrophys. **434** 971 (2005).

[159] T. Ueta and M. Meixner, Astrophys. J. **586** 1338 (2003).

[160] S. Wolf, Computer Phy. Comm. **150** 99 (2003).

[161] J. Steinacker, T. Henning, A. Bacmann and D. Semenov, Astron. Astrophys. **401** 405 (2003).

[162] T. Henning and R. Stognienko, Astron. Astrophys. **311** 291 (1996).

[163] B.Å.S. Gustafson and L. Kolokolova, J. Geophys. Res. **104** 31711 (1999).

[164] G. Wurm and M. Schnaiter, Astrophys. J. **567** 370 (2002).

[165] G. Wurm, H. Relke, J. Dorschner and O. Krauß, J. Quantitative Spect. and Radiative Transfer **89** 371 (2004).

[166] R.P. Nelson and J.C.B. Papaloizou, Mon. Not. Roy. Astr. Soc. **339** 993 (2003).

[167] O. Krauß and G. Wurm, Astrophys. J. **630** 1088 (2005).

[168] G. Wurm and O. Krauß, Icarus **180** 487 (2006).

[169] S. Beresnev, V. Chernyak and G. Fomyagin, Phys. Fluids A **5** 2043 (1993).

[170] J. Steinbach, J. Blum and M. Krause, Eur. Phys. J. E **15** 287 (2004).